

U-PINet: Physics-Informed Hierarchical Learning for Radar Cross Section Prediction via 3D Electromagnetic Scattering Reconstruction

Rui Zhu , *Student Member, IEEE*, Yuexing Peng , *Member, IEEE*, George C. Alexandropoulos , *Senior Member, IEEE*, Peng Wang , *Member, IEEE*, Wenbo Wang , *Senior Member, IEEE*, and Wei Xiang , *Senior Member, IEEE*

Abstract—Conventional computational electromagnetics (CEM) solvers can deliver high fidelity radar cross section (RCS) signatures by first solving the induced surface currents on 3-dimensional (3D) targets and then evaluating the scattered fields via radiation integrals. However, their computational cost becomes prohibitive for repeated queries and large-scale 3D scenarios. Recent purely data-driven networks improve efficiency, yet they often bypass this scattering mechanism, which may compromise physical consistency and generalization. To bridge this gap, in this paper, we propose U-PINet, a fully end-to-end, physics-informed hierarchical network for efficient RCS prediction via 3D electromagnetic scattering reconstruction. Once the scattering quantities are reconstructed, scattered fields and RCS can be evaluated for arbitrary observation directions via the radiation integral. U-PINet explicitly learns physics-consistent intermediate scattering representations by modeling local electromagnetic coupling and long-range radiation effects through a hierarchical operator design inspired by near-far field decomposition in fast solvers. A physics-guided graph neural network is incorporated to capture self- and mutual-coupling among mesh elements of complex targets, enabling physically interpretable intermediate representations. By embedding governing equations as residual constraints, U-PINet enables accurate object reconstruction of scattering quantities and consequently reliable RCS prediction across observation directions, while significantly reducing runtime. Extensive numerical experiments demonstrate that U-PINet achieves EM-solver-level RCS accuracy and 3D object reconstruction with orders of magnitude speedups, and generalizes well to unseen geometries under limited training data.

Index Terms—Computational electromagnetics, electromagnetic scattering, graph neural networks, physics-informed neural networks, radar cross section.

I. INTRODUCTION

RADAR cross section (RCS) computation plays a fundamental role in radar engineering and electromagnetic

(EM) analysis, serving as a primary descriptor of target scattering characteristics for detection [1], recognition [2], and signature evaluation [3]. Accurate RCS prediction establishes the quantitative relationship between the incident EM waves and the physical properties of scattering targets [4]. From a physics standpoint, RCS constitutes an engineering-level observable that follows from the underlying EM scattering quantities, most notably the induced surface currents governed by Maxwell’s equations [5]. Once these induced currents are obtained, the scattered field can be evaluated for arbitrary observation directions via radiation integrals, from which the corresponding RCS is deduced. Therefore, accurate 3-dimensional (3D) EM scattering reconstruction of the induced currents is key enabler for fast and high fidelity RCS prediction.

Classical computational electromagnetics (CEM) methods, such as the Method of Moments (MoM) [6], Finite Element Method (FEM) [7], and Finite-Difference Time-Domain (FDTD) [8], have been extensively investigated, demonstrating high accuracy in modeling EM scattering phenomena. Among these techniques, MoM has been particularly efficient for handling targets with complex geometries [9], providing increased accuracy, making it a widely adopted tool for high fidelity EM scattering reconstruction and subsequent RCS evaluation. In addition, to alleviate the computational burden associated with dense matrix operations in large-scale RCS computation cases, structural algorithmic enhancements of MoM [10], [11] in conjunction with the utilization of high-performance computing platforms [12], [13] have been proposed. The Multilevel Fast Multipole Algorithm (MLFMA) [14] introduces a hierarchical decomposition with near-/far-field partitioning to significantly reduce the computational complexity of MoM-based solvers, thereby accelerating the evaluation of long-range radiation effects that underpin scattered fields and RCS signatures. Further developments in kernel compression and fast matrix–vector multiplication [15]–[17] have enabled more efficient evaluation of far-field interactions and reduced memory consumption. However, despite these notable improvements, classical solvers remain challenged by their high computational cost and limited flexibility, and particularly in RCS analysis involving large-scale 3D targets, multi-aspect scanning, or repeated evaluations. Such scenarios are common in practical radar applications, yet the deterministic structure and matrix-based formulation of conventional solvers fundamentally constrain their scalability and efficiency.

In recent years, deep learning techniques have been explored as an alternative paradigm for accelerating EM scattering

This work was supported in part by the National Natural Science Foundation of China under Grant 62371066 and Science and Technology Innovation Program of Xiongan New Area (Grant No.2025XAGG0052). (*Corresponding author: Yuexing Peng*)

R. Zhu, Y. Peng, and W. Wang are with the Key Laboratory of Universal Wireless Communication, Ministry of Education (MoE), School of Information and Communication Engineering, Beijing University of Posts and Telecommunications, Beijing 100876, China (e-mail: {rayyyy, yxpeng, wbwang}@bupt.edu.cn).

G. C. Alexandropoulos is with the Department of Informatics and Telecommunications, National and Kapodistrian University of Athens, 16122 Athens, Greece (email: alexandg@di.uoa.gr).

P. Wang is with a telecommunication company in Stockholm, Sweden (e-mail: wp_ady@hotmail.com).

W. Xiang is with the School of Computing, Engineering and Mathematical Sciences, La Trobe University, Melbourne, VIC 3086, Australia (e-mail: w.xiang@latrobe.edu.au).

prediction and RCS computation. By leveraging their strong nonlinear approximation capability, neural networks can learn complex scattering behaviors from data and provide rapid inference once trained. Various end-to-end learning frameworks have been proposed to infer EM responses directly from geometric representations, including supervised descent approaches mapping image-based target descriptions to scattering characteristics [18], multi-task learning architectures that enhance generalization via shared latent spaces [19], and models incorporating extended input modalities such as radiation-direction maps [20]. Moreover, specific network architectures have been tailored for efficient field solving: fully convolutional networks (ConvNet) have been applied to predict potential distributions in 3D models with high numerical accuracy [21], while physics-augmented U-Net structures have been utilized to ensure physical consistency in EM field prediction [22]. However, most existing learning-based approaches for RCS and EM scattering prediction operate without explicit physical constraints. As a consequence, they function as black-box predictors whose internal representations lack correspondence to underlying EM principles. This deficiency raises concerns regarding their reliability and generalization, especially for targets with complex geometries or under unseen EM configurations [23]. Therefore, despite their promising efficiency, purely data-driven models remain insufficient for physically sensitive RCS computation tasks.

To overcome the computational and generalization challenges in EM scattering reconstruction, Physics-Informed Neural Networks (PINNs) [24] have been proposed to embed Maxwell’s equations and boundary conditions directly into the learning framework, thereby constraining the solution space to physically consistent regimes. Typically, PINNs enforce physical laws by incorporating governing equations into the loss function or by coupling neural networks with physics-based operators, such that the learned representations adhere to EM principles throughout training and inference. From an RCS perspective, this physics-informed paradigm is especially beneficial, as it not only stabilizes intermediate field or current predictions but also enhances the fidelity and robustness of the resulting far-field scattering signatures, enabling accurate RCS curve prediction with reduced training data.

In EM scattering problems, several studies have combined PINN-style formulations with classical solvers to accelerate simulations while preserving physical fidelity [25]–[27]. In [28], a learning framework is designed to mimic the update pattern of classical iterative schemes by alternately refining induced currents and material parameters, thus accelerating convergence under EM constraints, which is beneficial for subsequent far-field evaluation. In [29], deep generative models are regularized by conductivity–response relationships so that reconstructed images remain consistent with the underlying physics, improving stability in inverse scattering. The work in [30] approximates the integral operator using neural networks to rapidly estimate field distributions in two-dimensional configurations, which can further support fast scattering–response evaluation. To reduce the cost of dense matrix operations, [31] introduces residual correction driven by the volume integral equation, while [32] employs graph convolutional

neural networks (Graph-CNNs) to learn the structure of the Electric Field Integral Equation (EFIE), enabling data-driven approximations of field interactions with preserved physical semantics. In addition, [33] replaces conventional residual computation in 3D MoM solvers with a graph neural network module that models local interactions on mesh-based graphs and performs data-driven residual updates during the iterative process. Although these approaches significantly reduce the computational burden of solver iterations, their final objective is still largely tied to field- or current-level acceleration, and the RCS curve is typically obtained as a downstream quantity through additional far-field post-processing.

Other efforts extend physics-informed learning to multilevel fast algorithms. Under the MLFMA framework, the far-field translation operator has been approximated by radial basis function networks to capture long-range interactions between distant clusters. Building on this idea, [34] proposes a hybrid deep model that jointly trains multilevel translation operators through an embedding layer and a self-attention mechanism, enabling the automatic learning of dependencies across hierarchical levels [35]. The learning-assisted framework in [36] further accelerates MLFMA translation operations by learning EM interactions in a coarse-to-fine manner, reducing computational complexity for large-scale scattering problems. These developments indicate that physics-guided learning can effectively accelerate the evaluation of long-range radiation effects, which are directly related to the formation of multi-aspect far-field signatures and thus the resulting RCS curves.

Overall, existing PINN-based EM solvers inject physical priors, but remain tethered to conventional pipelines. This implies that mesh generation, matrix assembly, and iterative residual updates still dominate cost, making multi-aspect RCS calculation and repeated evaluations particularly inefficient. Motivated by this fact, in this paper, we propose U-PINet, a fully end-to-end physics-informed hierarchical framework that reconstructs the induced surface currents and then obtains the scattered fields and RCS signatures via the governing radiation formulations for arbitrary observation directions, thereby supporting diverse sensing geometries, while replacing classical solvers with physically consistent and scalable inference. The main technical contributions are summarized as follows.

- A physics-guided graph neural network (GNN) is developed, which serves as a near-field coupling engine efficiently capturing self- and mutual-interactions among mesh elements and producing physically interpretable local current representations.
- A hierarchical near-/far-field fusion operator with multiscale encoding and skip connections is introduced to integrate the learned near-field couplings with long-range radiation effects. This operator enables reconstructing the induced surface currents, yielding stable scattered field and RCS evaluation via the radiation integral across arbitrary observation directions.
- Our extensive numerical experiments demonstrate that U-PINet achieves EM-solver-level accuracy for both induced-current reconstruction and RCS prediction with orders of magnitude runtime reduction, offering also strong generalization.

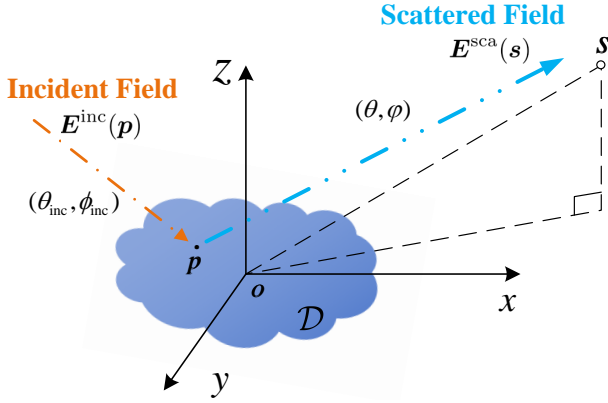


Fig. 1. Geometry for EM scattering and RCS evaluation. A PEC target with surface \mathcal{D} (point \mathbf{p} belongs in this surface) is illuminated by an incident plane wave \mathbf{E}^{inc} from direction $(\theta_{\text{inc}}, \phi_{\text{inc}})$, and the scattered field \mathbf{E}^{sca} is observed at a far-field point \mathbf{s} along the direction (θ, ϕ) .

The remainder of the paper is organized as follows. Section II reviews the MLFMA foundations and introduces the proposed U-PINet principle discussing its core feature of preserving physical structure while avoiding solver-dependent bottlenecks. Section IV outlines the proposed physics-guided neural network architecture for 3D EM scattering reconstruction, in particular, its near-field graph module and the hierarchical far-field learning mechanism. Section V introduces our experimental setup and Section VI presents a series of experiments assessing our U-PINet’s reconstruction performance. Section VII concludes the paper and highlights future research directions.

II. PROBLEM FORMULATION AND STATE OF THE ART

A. Scattered Electric Field and Radar Cross Section

Consider a representative perfectly electrically conducting (PEC) target with surface \mathcal{D} embedded in a homogeneous background medium, as illustrated in Fig. 1. Without loss of generality, we adopt a 3D Cartesian coordinate system with the target centered at the origin \mathbf{o} . The target is illuminated by a prescribed incident plane wave \mathbf{E}^{inc} impinging from direction $(\theta_{\text{inc}}, \phi_{\text{inc}})$, and the scattered response is observed at an exterior far-field point \mathbf{s} parameterized by range-angle coordinates as $\mathbf{s} = s(\sin \theta \cos \phi, \sin \theta \sin \phi, \cos \theta)$. Under far-field conditions ($s \rightarrow \infty$), $\|\mathbf{s} - \mathbf{p}\|_2 \approx s$ holds for all $\mathbf{p} \in \mathcal{D}$, so the observation is fully characterized by the angles (θ, ϕ) .

Let $\mathbf{p}, \mathbf{p}' \in \mathcal{D}$ denote a surface testing point and a surface source (integration) point on the target, respectively. According to EM theory, the tangential component of the total electric field must vanish on the PEC surface \mathcal{D} . Using $\hat{\mathbf{n}}(\mathbf{p})$ to denote the outward unit normal vector at the testing point $\mathbf{p} \in \mathcal{D}$, this boundary condition is mathematically expressed as follows:

$$\hat{\mathbf{n}}(\mathbf{p}) \times (\mathbf{E}^{\text{inc}}(\mathbf{p}) + \mathbf{E}^{\text{sca}}(\mathbf{p})) = \mathbf{0}. \quad (1)$$

Enforcing this condition together with the radiation condition yields the EFIE. Specifically, under a prescribed incident field

$\mathbf{E}^{\text{inc}}(\mathbf{p})$, the induced surface current density $\mathbf{J}(\cdot)$ satisfies the following expression $\forall \mathbf{p} \in \mathcal{D}$:

$$\int_{\mathbf{p}' \in \mathcal{D}} \mathbf{G}(\mathbf{p}, \mathbf{p}') \mathbf{J}(\mathbf{p}') d\mathbf{p}' = \mathbf{E}^{\text{inc}}(\mathbf{p}), \quad (2)$$

where $\mathbf{G}(\cdot, \cdot)$ denotes the dyadic Green’s function kernel in the background medium [37]. The induced surface current density $\mathbf{J}(\cdot)$ is the unknown quantity to be solved for in (2).

Once the induced surface current density \mathbf{J} is obtained, the scattered field can be evaluated at an arbitrary exterior observation point \mathbf{s} via the radiation integral:

$$\mathbf{E}^{\text{sca}}(\mathbf{s}) = \int_{\mathbf{p} \in \mathcal{D}} \mathbf{G}(\mathbf{s}, \mathbf{p}) \mathbf{J}(\mathbf{p}) d\mathbf{p}. \quad (3)$$

The corresponding RCS at (θ, ϕ) is then defined as [4]:

$$\sigma(\theta, \phi) = \lim_{s \rightarrow \infty} \left(4\pi s^2 \left| \frac{\mathbf{E}^{\text{sca}}(\mathbf{s})}{\mathbf{E}^{\text{inc}}(\mathbf{o})} \right|^2 \right), \quad (4)$$

where $\mathbf{E}^{\text{inc}}(\mathbf{o})$ denotes the amplitude of the incident plane wave at the origin. It is noted that different sensing setups are implied through different combinations of the illumination and observation directions. Monostatic RCS corresponds to the backscattering direction of $(\theta_{\text{inc}}, \phi_{\text{inc}})$, whereas bistatic/multistatic configurations simply correspond to other receive directions. Therefore, once the induced surface current \mathbf{J} is accurately reconstructed, the RCS can be evaluated for arbitrary observation angles via the radiation integral.

B. The MLFMA Framework

To motivate the methodological structure underlying our model design, we briefly overview the physics-based computational paradigm of MLFMA [14]. As indicated by (2)–(4), accurate evaluation of the RCS signature $\sigma(\theta, \phi)$ requires the induced surface current \mathbf{J} , which is obtained by solving the EFIE in (2). To this end, expression (2) can be discretized using the Rao–Wilton–Glisson (RWG) basis functions defined on mesh edges [38]. The resulting MoM formulation yields a dense linear system $\mathbf{Z}\mathbf{I} = \mathbf{V}$, whose direct matrix–vector products scale as $\mathcal{O}(N^2)$, with N denoting the number of unknown degrees of freedom, i.e., the number of RWG basis functions (typically on the order of the number of interior mesh edges). In the latter system, $\mathbf{Z} \in \mathbb{C}^{N \times N}$ is the impedance matrix, $\mathbf{I} \in \mathbb{C}^N$ collects the RWG expansion coefficients of the induced surface current, and $\mathbf{V} \in \mathbb{C}^N$ contains the tested incident field. To enable fast evaluation in the MLFMA, the impedance matrix is decomposed as follows:

$$\mathbf{Z} = \mathbf{Z}_{\text{near}} + \mathbf{Z}_{\text{far}}, \quad (5)$$

where \mathbf{Z}_{near} contains all interactions between geometrically close basis functions and \mathbf{Z}_{far} accounts for the remaining long-range terms.

From a structural viewpoint, MLFMA is essentially built on the interplay between near-field accurate interaction, far-field multilevel evaluation, and the residual-driven iterative solver of the EFIE, forming a unified computational flow that preserves full EM physics while reducing complexity. First, pairs of basis functions whose supports are geometrically close

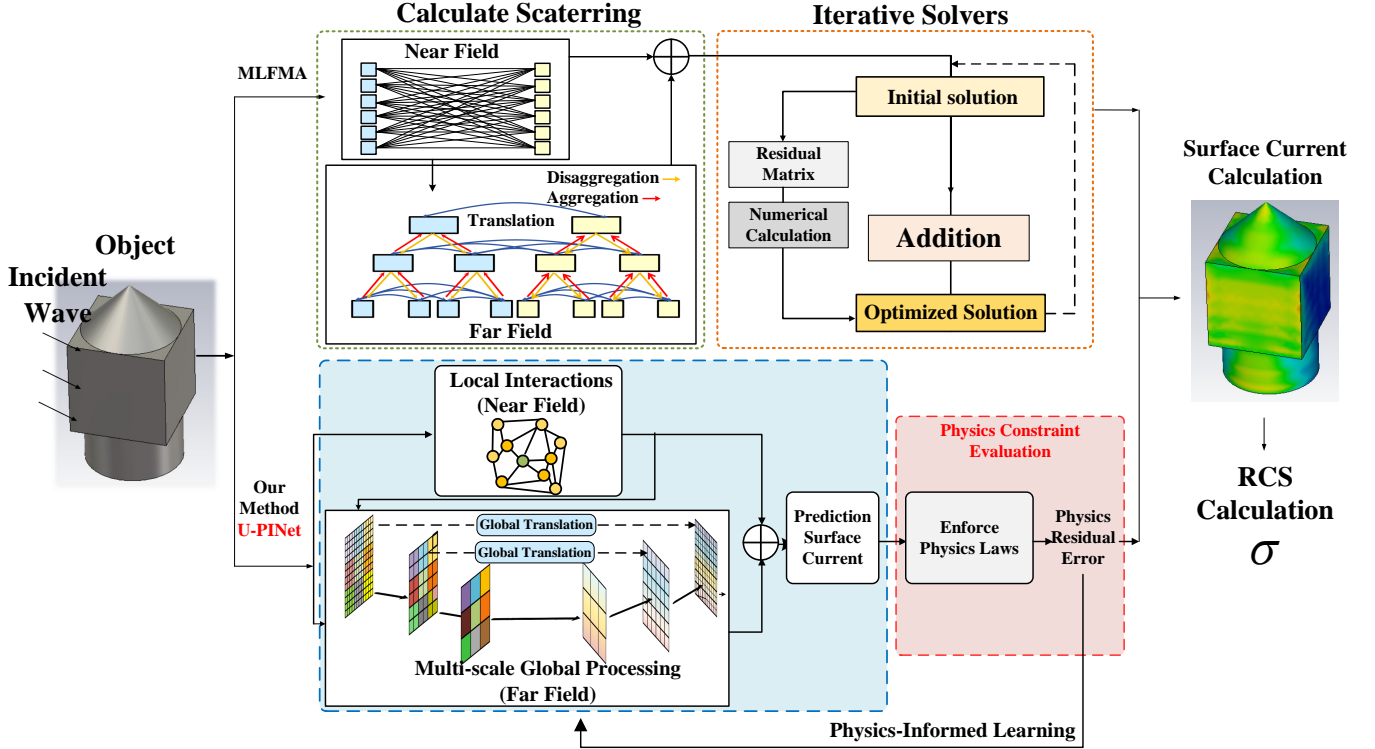


Fig. 2. The RCS, $\sigma(\theta, \phi)$, calculation procedure using the standard MLFMA framework [14] (top) and the proposed U-PINet (bottom), which utilizes physics-informed learning to directly resolve field interactions. In this way, traditional iterative solvers are bypassed enabling to rapidly determine the scattered field for the desired RCS assessment. U-PINet’s core components and overall architecture are detailed in Sections III and IV.

are collected in the near-neighbor list \mathcal{N} , and its contributions are computed exactly to form the near-field impedance block \mathbf{Z}_{near} . This block contributes the term $\mathbf{Z}_{\text{near}}\mathbf{I}$, which captures local self and mutual coupling in a purely MoM. Second, the far-field interactions are organized on an L -level octree [39]. At each level l ($l = 1, \dots, L$), the outgoing radiation patterns $\beta^{(l)}$ of source groups are first aggregated to the parent level through a phase-shifted combination of child patterns. For each group, well-separated interactions are handled by a translation operator \mathcal{T}_l , which maps the aggregated patterns $\beta^{(l)}$ of groups in the interaction list \mathcal{I} to incoming fields $\alpha_{\text{trans}}^{(l)}$. At the end of this multilevel evaluation, the finest-level translated field $\alpha^{(L)}$ yields the far-field contribution of the MoM matrix–vector product, denoted as $\mathbf{Z}_{\text{far}}\mathbf{I}$. Together with the exactly computed near-field term $\mathbf{Z}_{\text{near}}\mathbf{I}$, MLFMA reconstructs the full matrix–vector multiplication

$$\mathbf{Z}\mathbf{I} = (\mathbf{Z}_{\text{near}} + \mathbf{Z}_{\text{far}})\mathbf{I}.$$

Finally, this residual is then used by an iterative Krylov solver (e.g., GMRES [40] or BiCGStab [41]) to update the current vector \mathbf{I} until the boundary condition is satisfied, completing the residual-driven enforcement of the EFIE within the MLFMA framework. After convergence, the solved coefficient vector \mathbf{I} is substituted back into the RWG expansion to recover the induced surface current $\mathbf{J}(\cdot)$. The scattered field is then evaluated via (3), and the desired bistatic RCS signature $\sigma(\theta, \phi)$ is obtained by evaluating expression (4).

Algorithm 1 summarizes MLFMA’s physically structured data flow, which serves as a reference model for the design of

our physics-guided near–far learning architecture in U-PINet.

III. THE PROPOSED U-PINET FRAMEWORK

To enable efficient and physically consistent RCS evaluation, the proposed U-PINet, whose overall architecture is presented in the following Section IV, capitalizes on the near–far organization of MLFMA while directly targeting accurate far-field scattering responses, as illustrated in Fig. 2. Algorithm 2 summarizes the overall procedure, and the following subsections describe its key steps: *Near-Field Interaction Learning* corresponds to Steps 1 and 2; *Far-Field Interaction Learning* corresponds to Stages 3–5; *Physics-Informed Residual Error* corresponds to Step 6; and the final scattered-field/RCS evaluation corresponds to Step 7.

1) *Near-Field Interaction Learning*: To model near-field interactions in a MoM-consistent manner, we construct a graph on the discretized surface points. For each surface node (testing point) $\mathbf{p}_i \in \mathcal{P}$, its neighborhood is defined as follows:

$$\mathcal{N}(i) = \{j : \|\mathbf{p}_i - \mathbf{p}_j\| \leq r_{\text{nf}}\}, \quad (6)$$

where r_{nf} denotes the near-field interaction radius chosen proportional to the local electrical size to capture strong short-range EM coupling. This expression implies that $\mathcal{N}(i)$ gathers the geometrically nearby points that dominate self/mutual coupling, mirroring the near-field interaction list in MoM-based discretizations. On each edge (i, j) , we define a physics-guided edge feature as follows:

$$\mathbf{w}_{ij} = \mathcal{G}(\|\mathbf{p}_i - \mathbf{p}_j\|, \mathbf{n}_i - \mathbf{n}_j), \quad (7)$$

Algorithm 1 The MLFMA Approach

Require: Mesh basis functions $\{\mathbf{f}_n\}$; Tree levels L , Translation Operator \mathcal{T} , the tested incident field \mathbf{V} , Observation angles (θ, ϕ) .

Ensure: Current coefficients \mathbf{I} satisfying boundary conditions.

Step 1: Octree Construction

- 1: Partition mesh into hierarchical groups from Level 1 (Root) to L (Leaves)
- 2: Identify Near-neighbors \mathcal{N} and Interaction list \mathcal{I} for each group

Step 2: Near-Field Interaction

- 3: Compute the MoM: $\mathbf{Z}_{\text{near}}\mathbf{I}$

Stage 3: Aggregation

- 4: Compute radiation patterns at leaves: $\beta^{(L)} \leftarrow \mathcal{F}(\mathbf{I})$

- 5: **for** $l = L$ down to 2 **do**

- 6: $\beta^{(l-1)} \leftarrow \sum_{\text{child}} \text{Interp}(\beta^{(l)} \cdot e^{jk \cdot d})$

- 7: **end for**

Stage 4: Translation

- 8: **for** $l = 2$ to L **do**

- 9: $\alpha_{\text{trans}}^{(l)} \leftarrow \sum_{m \in \mathcal{I}} \mathcal{T}_l \cdot \beta_m^{(l)}$

- 10: **end for**

Stage 5: Disaggregation

- 11: Initialize root field $\alpha^{(1)} \leftarrow 0$

- 12: **for** $l = 2$ to L **do**

- 13: $\alpha^{(l)} \leftarrow \text{Anterp}(\alpha^{(l-1)} \cdot e^{-jk \cdot d}) + \alpha_{\text{trans}}^{(l)}$

- 14: **end for**

- 15: $\mathbf{Z}_{\text{far}}\mathbf{I} \leftarrow \int \alpha^{(L)}(\hat{\mathbf{k}}) \cdot \mathbf{f}(\hat{\mathbf{k}}) d\hat{\mathbf{k}}$

Step 6: Iterative Solver Update

- 16: $\mathbf{Z}\mathbf{I} = \mathbf{Z}_{\text{near}}\mathbf{I} + \mathbf{Z}_{\text{far}}\mathbf{I}$

- 17: Compute Residual: $\mathbf{r} \leftarrow \mathbf{V} - \mathbf{Z}\mathbf{I}$

- 18: Update \mathbf{I} via GMRES/BiCGStab to minimize $\|\mathbf{r}\|$

Step 7: Scattered Field and RCS Evaluation

- 19: Recover \mathbf{J} from the converged coefficients \mathbf{I}

- 20: Compute \mathbf{E}^{sca} via (3) and obtain $\sigma(\theta, \phi)$ by (4)

where $\mathcal{G}(\cdot)$ encodes the dependence of the Green's function on inter-point distance and normal alignment. This design turns the edge attributes into a learnable surrogate of the self and mutual impedance terms in MoM, while preserving its geometric and EM structure.

On the constructed graph, the near-field module of U-PINet updates the current at node \mathbf{p}_i through an iterative message-passing scheme as:

$$\mathbf{J}^{(t+1)}(\mathbf{p}_i) = \mathbf{J}^{(t)}(\mathbf{p}_i) + \sum_{j \in \mathcal{N}(i)} h_t(\mathbf{w}_{ij}, \mathbf{J}^{(t)}(\mathbf{p}_j)), \quad (8)$$

where $h_t(\cdot)$ is a learnable local kernel at iteration t that transforms the message from neighbor j to node i based on the edge feature \mathbf{w}_{ij} and the neighbor current $\mathbf{J}^{(t)}(\mathbf{p}_j)$. Structurally, (8) follows the same aggregation pattern as the MoM near-field operator, i.e.:

$$[\mathbf{Z}_{\text{near}}\mathbf{I}]_i = \sum_{j \in \mathcal{N}(i)} [\mathbf{Z}_{\text{near}}]_{i,j} [\mathbf{I}]_j, \quad (9)$$

Algorithm 2 Proposed Physics-Guided Near-Far Field Scheme

Require: Discrete point set $\mathcal{P} = \{\mathbf{p}_i\}$ with normals $\{\mathbf{n}_i\}$; Radius r_{nf} , Levels L , Incident field \mathbf{E}^{inc} , Observation angles (θ, ϕ) .

Ensure: Predicted surface current \mathbf{J}_{pred} .

Step 1: Near-Field Graph Construction

- 1: **for** each point $\mathbf{p}_i \in \mathcal{P}$ **do**

- 2: Find neighbors: $\mathcal{N}(i) \leftarrow \{j : \|\mathbf{p}_i - \mathbf{p}_j\| \leq r_{\text{nf}}\}$

- 3: Compute edge weights: $\mathbf{w}_{ij} \leftarrow \mathcal{G}(\|\mathbf{p}_i - \mathbf{p}_j\|, \mathbf{n}_i - \mathbf{n}_j)$

- 4: **end for**

Step 2: Iterative Near-Field Update

- 5: Initialize $\mathbf{J}^{(0)}(\mathbf{p}_i)$

- 6: **for** $t = 0$ to $T_{\text{iter}} - 1$ **do**

- 7: $\mathbf{J}^{(t+1)}(\mathbf{p}_i) \leftarrow \mathbf{J}^{(t)}(\mathbf{p}_i) + \sum_{j \in \mathcal{N}(i)} h_t(\mathbf{w}_{ij}, \mathbf{J}^{(t)}(\mathbf{p}_j))$

- 8: **end for**

- 9: $\mathbf{J}_{\text{near}}(\mathbf{p}_i) \leftarrow \mathbf{J}^{T_{\text{iter}}}(\mathbf{p}_i)$

Step 3: Hierarchical Source Aggregation

- 10: Construct partition $\{\mathcal{C}^{(k)}\}_{k=1}^L$ from \mathcal{P}

- 11: Set finest level source: $\mathbf{S}^{(L)} \leftarrow \mathbf{J}^{T_{\text{iter}}}$

- 12: **for** $k = L$ down to 2 **do**

- 13: $\mathbf{S}^{(k-1)} \leftarrow \text{Pooling}(\mathbf{S}^{(k)})$

- 14: **end for**

Stage 4: Global Translation via Cross-Scale Attention

- 15: **for** $k = 2$ to L **do**

- 16: $\tilde{\mathbf{S}}^{(k)} \leftarrow \text{Attn} \left(\underbrace{\mathbf{S}^{(k)}}_{\text{Observation (Q)}}, \underbrace{\text{Unpooling}(\tilde{\mathbf{S}}^{(k-1)})}_{\text{Global Source (K,V)}} \right)$

- 17: **end for**

Stage 5: Hierarchical Field Disaggregation

- 18: **for** $k = 2$ to L **do**

- 19: $\mathbf{J}_{\text{far}}^{(k)} \leftarrow \tilde{\mathbf{S}}^{(k)} + \sum_{n=1}^{N_{\text{kem}}} \mathbf{W}_n \cdot \mathbf{J}_{\text{far}}^{(k-1)}$

- 20: **end for**

- 21: $\mathbf{J}_{\text{far}}(\mathbf{p}_i) \leftarrow \mathbf{J}_{\text{far}}^{(k)}$

Step 6: Residual Evaluation and Optimization

- 22: $\mathbf{J}_{\text{pred}}(\mathbf{p}_i) \leftarrow \mathbf{J}_{\text{near}}(\mathbf{p}_i) + \mathbf{J}_{\text{far}}(\mathbf{p}_i)$

- 23: $\mathbf{E}^{\text{sca}}(\mathbf{p}_i) \leftarrow \sum_j \mathbf{G}(\mathbf{p}_i, \mathbf{p}_j) \cdot \mathbf{J}_{\text{pred}}(\mathbf{p}_j)$

- 24: Enforce $\hat{\mathbf{n}} \times \mathbf{E}^{\text{total}} = 0$:

- 25: $\mathcal{L}_{\text{phys}} \leftarrow \mathbb{E}_{\mathbf{p}_i \in \mathcal{P}} \left[\left\| \hat{\mathbf{n}}_i \times (\mathbf{E}^{\text{inc}}(\mathbf{p}_i) + \mathbf{E}^{\text{sca}}(\mathbf{p}_i; \mathbf{J}_{\text{pred}})) \right\|^2 \right]$

- 26: Update trainable kernels Θ to minimize $\mathcal{L}_{\text{phys}}$

Step 7: Scattered Field and RCS Evaluation

- 27: Evaluate \mathbf{E}^{sca} from \mathbf{J}_{pred} via (3)

- 28: Compute the RCS signature $\sigma(\theta, \phi)$ according to (4)

where the contribution at index i is obtained by summing the weighted influence of its near-field neighbors. It is noted that, if we restrict h_t to be linear in $\mathbf{J}^{(t)}(\mathbf{p}_j)$, the message term can be written as follows:

$$h_t(\mathbf{w}_{ij}, \mathbf{J}^{(t)}(\mathbf{p}_j)) \approx K_t(i, j) \mathbf{J}^{(t)}(\mathbf{p}_j), \quad (10)$$

where $K_t(i, j)$ acts as an effective, data-driven near-field coefficient determined by the physics-guided edge feature \mathbf{w}_{ij} .

In this view, the update in (8) is precisely a graph neural network (GNN) [42] message-passing block. At each iteration t , the node associated with \mathbf{p}_i aggregates the current estimates $\{\mathbf{J}^{(t)}(\mathbf{p}_j)\}_{j \in \mathcal{N}(i)}$ of its near-field neighbors, weighs each contribution through the physics-guided kernel $h_t(\mathbf{w}_{ij}, \cdot)$, and

accumulates them to form a local correction. Structurally, this aggregation mirrors the MoM near-field matrix–vector product, where the i -th row of \mathbf{Z}_{near} collects and sums the influence of all neighboring basis functions on the i -th degree of freedom. As a result, the near-field module can be viewed as a MoM-informed GNN operator that performs physics-guided message passing on the mesh graph. It remains computationally efficient and adaptable across different geometries and tessellations, while staying tightly anchored to the underlying EM physics through the MoM-consistent neighborhood $\mathcal{N}(i)$ and the Green’s-function-based edge features w'_{ij} .

2) *Far-Field Interaction Learning*: To highlight how U-PINet is informed by the MLFMA structure, we first rewrite the far-field stages of Algorithm 1 in a compact operator form. On level l of the octree, the aggregation, translation, and disaggregation steps can be summarized as follows:

$$\boldsymbol{\beta}^{(l-1)} = \mathcal{A}_l(\boldsymbol{\beta}^{(l)}), \quad l = L, \dots, 2, \quad (11)$$

$$\boldsymbol{\alpha}_{\text{trans}}^{(l)} = \mathcal{T}_l(\{\boldsymbol{\beta}_m^{(l)}\}_{m \in \mathcal{I}}), \quad l = 2, \dots, L, \quad (12)$$

$$\boldsymbol{\alpha}^{(l)} = \mathcal{D}_l(\boldsymbol{\alpha}^{(l-1)}, \boldsymbol{\alpha}_{\text{trans}}^{(l)}), \quad l = 2, \dots, L, \quad (13)$$

where $\mathcal{A}_l(\cdot)$ denotes the level- l aggregation operator that interpolates and phase-shifts child radiation patterns into the parent pattern, $\mathcal{T}_l(\cdot)$ is the level-dependent translation operator that maps outgoing patterns $\boldsymbol{\beta}^{(l)}$ of well-separated groups to incoming fields $\boldsymbol{\alpha}_{\text{trans}}^{(l)}$, and $\mathcal{D}_l(\cdot, \cdot)$ performs disaggregation (interpolation and phase compensation) from coarse to fine levels. At the finest level, the accumulated incoming field is finally projected back to the testing basis functions to yield the far-field contribution:

$$\mathbf{Z}_{\text{far}} \mathbf{I} = \mathcal{R}(\boldsymbol{\alpha}^{(L)}), \quad (14)$$

where $\mathcal{R}(\cdot)$ represents the radiation operator that recovers the far-field part of the MoM matrix–vector product.

In U-PINet, the far-field branch also adopts a multilevel organization. Let $\mathbf{S}^{(k)}$ denote the source representation on level k produced by the near-field graph module. The hierarchical source aggregation in Algorithm 2 can be written in a compact form $\forall k = L, \dots, 2$ as follows:

$$\mathbf{S}^{(k-1)} = \Gamma_k(\mathbf{S}^{(k)}), \quad (15)$$

where $\Gamma_k(\cdot)$ is a pooling operator that aggregates fine-scale sources on level k into coarser descriptors on level $k-1$. This provides a learnable multilevel source compression, playing a role analogous in spirit to the aggregation stage of MLFMA.

To mimic the multilevel far-field translation of MLFMA in a learnable manner, U-PINet introduces a cross-scale attention block [43] at each hierarchy level. Given the level- k features $\mathbf{S}^{(k)}$ and the coarser representation $\tilde{\mathbf{S}}^{(k-1)}$, the global translation step is written as follows:

$$\tilde{\mathbf{S}}^{(k)} = \Phi_k(\mathbf{S}^{(k)}, \mathcal{U}_k(\tilde{\mathbf{S}}^{(k-1)})), \quad k = 2, \dots, L, \quad (16)$$

where $\Phi_k(\cdot, \cdot)$ denotes the learnable cross-scale translation block and $\mathcal{U}_k(\cdot)$ is an unpooling operator that lifts the coarse-level representation $\tilde{\mathbf{S}}^{(k-1)}$ to level k . In this formulation, $\mathbf{S}^{(k)}$ plays the role of level- k testing groups, while $\mathcal{U}_k(\tilde{\mathbf{S}}^{(k-1)})$

provides a global source context analogous to the multigroup far-field patterns in the MLFMA framework. Concretely, the block Φ_k is implemented as a cross-attention layer. Let

$$\mathbf{Q}^{(k)} = \mathbf{W}_Q^{(k)} \mathbf{S}^{(k)}, \quad (17)$$

$$\mathbf{K}^{(k)} = \mathbf{W}_K^{(k)} \mathcal{U}_k(\tilde{\mathbf{S}}^{(k-1)}), \quad (18)$$

$$\mathbf{V}^{(k)} = \mathbf{W}_V^{(k)} \mathcal{U}_k(\tilde{\mathbf{S}}^{(k-1)}), \quad (19)$$

where $\mathbf{Q}^{(k)}$, $\mathbf{K}^{(k)}$, and $\mathbf{V}^{(k)}$ denote the query, key, and value feature embeddings at level k , respectively, and $\mathbf{W}_Q^{(k)}$, $\mathbf{W}_K^{(k)}$, and $\mathbf{W}_V^{(k)}$ are trainable linear projection matrices that map the hierarchical source representations into a shared attention subspace for learning cross-scale EM interactions. For an observation group i and a source group m , the attention weight is given by the following expression:

$$a_{i,m}^{(k)} \triangleq \text{softmax}_m(\langle \mathbf{Q}_i^{(k)}, \mathbf{K}_m^{(k)} \rangle) = \frac{\exp(\langle \mathbf{Q}_i^{(k)}, \mathbf{K}_m^{(k)} \rangle)}{\sum_{m'} \exp(\langle \mathbf{Q}_i^{(k)}, \mathbf{K}_{m'}^{(k)} \rangle)}, \quad (20)$$

where $\langle \cdot, \cdot \rangle$ denotes the standard inner product between two feature vectors, $\exp(\cdot)$ is the exponential function, and $\text{softmax}_m(\cdot)$ denotes the softmax normalization over all source groups indexed by m [43]. The updated representation of group i is then obtained as follows:

$$\tilde{\mathbf{S}}_i^{(k)} = \sum_m a_{i,m}^{(k)} \mathbf{V}_m^{(k)}. \quad (21)$$

In this way, the attention weights $a_{i,m}^{(k)}$ function as a learned analogue of the MLFMA translation kernel $T_l(i, m)$, while the value vectors $\mathbf{V}_m^{(k)}$ serve as learnable far-field source patterns; together with the hierarchy, the block Φ_k provides a physics-guided neural counterpart of the classical multilevel far-field translation process. The far-field current contribution is then recovered through a hierarchical disaggregation step,

$$\mathbf{J}_{\text{far}}^{(k)} = \Psi_k(\mathbf{J}_{\text{far}}^{(k-1)}, \tilde{\mathbf{S}}^{(k)}), \quad k = 2, \dots, L, \quad (22)$$

where $\Psi_k(\cdot, \cdot)$ denotes a learnable kernel-fusion operator that injects the translated source features $\tilde{\mathbf{S}}^{(k)}$ into the level- k far-field current. At the finest level, the predicted far-field current is given as follows:

$$\mathbf{J}_{\text{far}} = \mathbf{J}_{\text{far}}^{(L)}, \quad (23)$$

which serves as the neural counterpart of the far field and is combined with the near-field graph output in the physics loss.

Comparing (11)-(14) with (15)-(22), U-PINet preserves the same near–far information flow as MLFMA: fine-to-coarse aggregation, level-wise translation, and coarse-to-fine reconstruction. The crucial change offered by U-PINet is that the fixed analytical operators ($\mathcal{A}_l, \mathcal{T}_l, \mathcal{D}_l, \mathcal{R}$) are now replaced by learnable counterparts (Γ_k, Φ_k, Ψ_k).

3) *Physics-Informed Residual Error*: The residual enforcement in U-PINet mirrors the residual-driven update mechanism found in the classical MLFMA pipeline. Specifically, the proposed network outputs a predicted surface current density, decomposed into near- and far-field components as $\mathbf{J}_{\text{pred}} = \mathbf{J}_{\text{near}} + \mathbf{J}_{\text{far}}$. Using this prediction, the scattered electric field

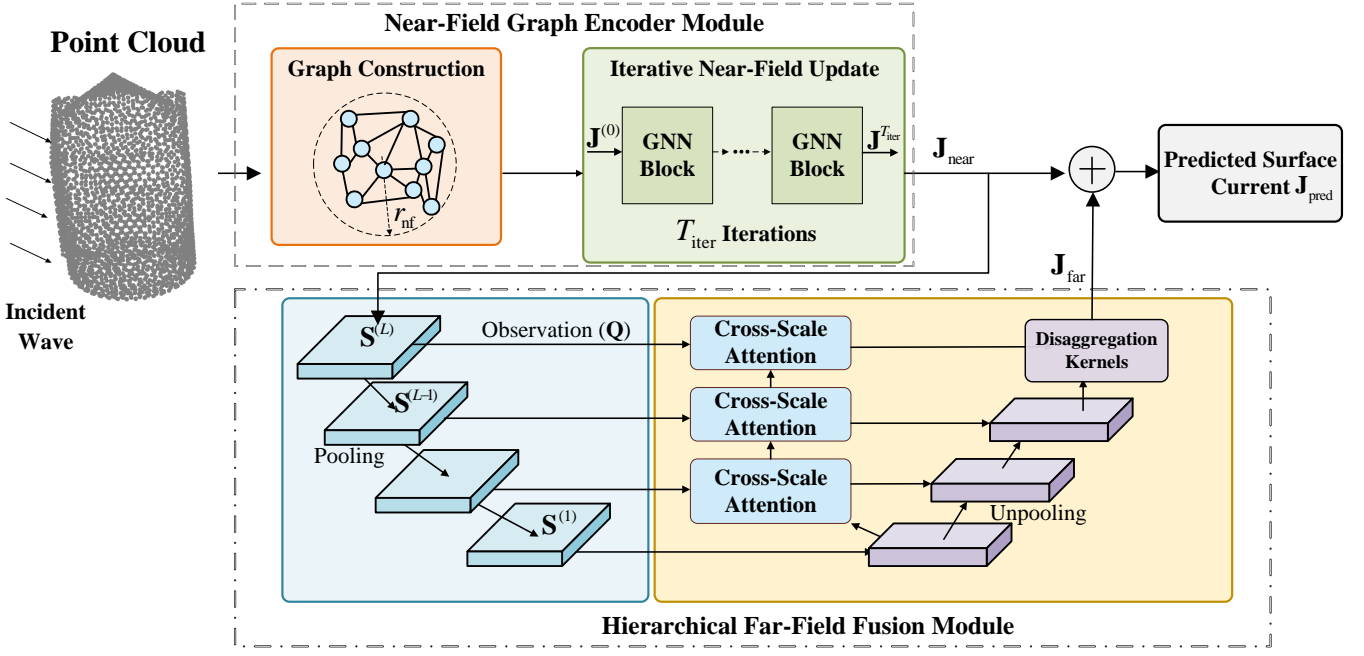


Fig. 3. The architecture of the proposed U-PINet for physics-informed surface current prediction.

is then reconstructed via the dyadic Green's function integral as expressed in (3). To ensure physical consistency, the PEC boundary condition formulated in (1) is directly enforced by minimizing the following physics-informed residual loss:

$$\mathcal{L}_{\text{phys}} = \mathbb{E}_{\mathcal{P}} \left[\left\| \hat{\mathbf{n}}_i \times (\mathbf{E}^{\text{inc}}(\mathbf{p}_i) + \mathbf{E}^{\text{sca}}(\mathbf{p}_i; \mathbf{J}_{\text{pred}})) \right\|^2 \right], \quad (24)$$

where \mathcal{P} denotes the set of collocation points on the discretized surface, i.e., $\mathbf{p}_i \in \mathcal{P} \forall i$, over which the expectation is taken.

In contrast to the classical MLFMA, where the residual drives a Krylov subspace solver (e.g., GMRES or BiCGStab) to iteratively update the current coefficients, U-PINet utilizes $\mathcal{L}_{\text{phys}}$ to optimize the trainable parameters of the hierarchical near-far architecture. This training process ensures that a single forward pass produces a current distribution \mathbf{J}_{pred} that approximately satisfies the EFIE. Consequently, the physics-informed loss in U-PINet plays a role analogous to the residual vector in methods based on iterative solvers, effectively closing the loop between near-field graph modeling, multilevel far-field coupling, and EM boundary-condition enforcement.

Finally, once the network is trained, the resulting \mathbf{J}_{pred} is employed to evaluate the far-field scattering response via (3), and the final bistatic RCS signature $\sigma(\theta, \phi)$ is computed according to the far-field definition in (4).

IV. THE U-PINET NEURAL NETWORK ARCHITECTURE

In this section, we present the architecture of the proposed artificial neural network for physics-informed EM scattering reconstruction, where the induced surface current constitutes the primary learning target. As shown in Fig. 3, U-PINet takes the object geometry, surface normals, and incident field as inputs, and then outputs the predicted surface current \mathbf{J}_{pred} in an end-to-end, multi-stage manner that mirrors the near-far organization of MLFMA. The subsequent physics-based

mapping from \mathbf{J}_{pred} to the scattered field and the RCS signature, together with the physics-residual supervision used during training, is illustrated separately in Fig. 5.

A. Near-Field Graph Encoder Module

Following the near-field modeling in Section II, we construct a graph on the discretized surface points \mathcal{P} , with neighborhoods $\mathcal{N}(i)$ and physics-guided edge descriptors (7) as defined therein. In the network implementation, the point set and edge structure are kept the same, while the kernel $\mathcal{G}(\cdot)$ is instantiated by a dual-attention mechanism that produces learnable near-field coupling weights.

As shown in Fig. 4(a), the physics-guided edge kernel $\mathcal{G}(\cdot)$ is realized as an attention module that takes the geometric inputs and produces a near-field edge weight w_{ij} for each neighboring pair (i, j) . For each point \mathbf{p}_i , we estimate its local sampling density by Gaussian kernel [44] density estimation over $\mathcal{N}(i)$, as follows:

$$\hat{f}(\mathbf{p}_i) = \frac{1}{N h (2\pi)^{3/2}} \sum_{j \in \mathcal{N}(i)} \exp\left(-\frac{1}{2} \left\| \frac{\mathbf{p}_i - \mathbf{p}_j}{h} \right\|^2\right), \quad (25)$$

where $N = |\mathcal{N}(i)|$ and $h > 0$ is the kernel bandwidth with $\mathcal{K}(\mathbf{x}) = \exp(-\|\mathbf{x}\|^2/2)$. The inverse density is given by:

$$\mathcal{D}(\mathbf{p}_i) = \frac{1}{\hat{f}(\mathbf{p}_i)}, \quad (26)$$

which is normalized and mapped to a density-based attention:

$$\mathcal{D}_{\text{norm}}(\mathbf{p}_j) = \frac{\mathcal{D}(\mathbf{p}_j)}{\max_{\ell} \mathcal{D}(\mathbf{p}_{\ell})}, \quad s_{ij}^{\text{den}} = F_d(\mathcal{D}_{\text{norm}}(\mathbf{p}_j)), \quad (27)$$

$$\beta_{ij} = \frac{\exp(s_{ij}^{\text{den}})}{\sum_{j' \in \mathcal{N}(i)} \exp(s_{ij'}^{\text{den}})}, \quad (28)$$

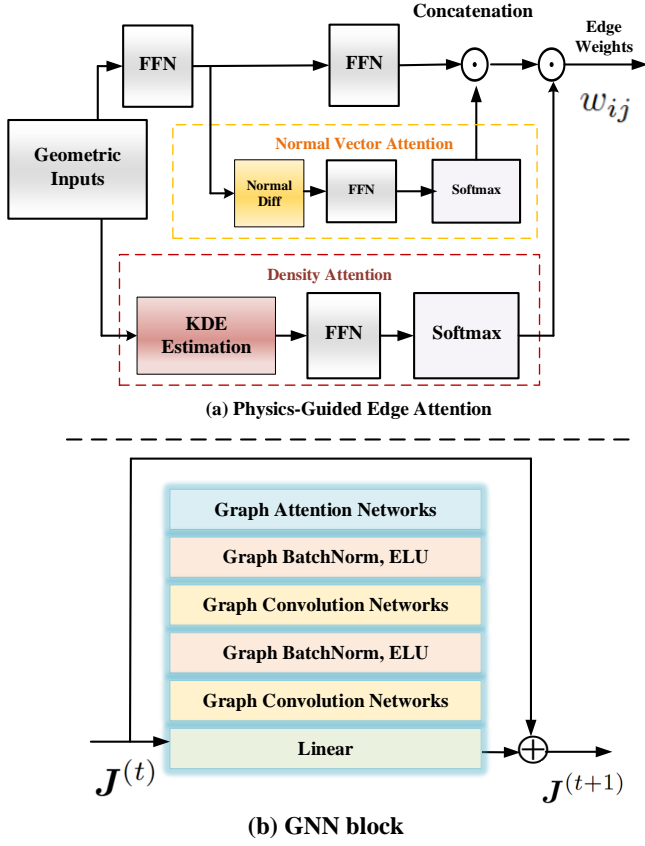


Fig. 4. (a) Physics-guided edge attention combining density- and normal-based branches to produce learnable near-field edge weights; (b) GNN block that stacks GAT/GCN layers to iteratively refine the surface current.

where $F_d(\cdot)$ is a two-layer feed-forward (FF) network. Local geometric anisotropy is encoded by the difference of unit normals $\Delta \mathbf{n}_{ij} = \mathbf{n}_i - \mathbf{n}_j$, yielding the normal-based attention:

$$s_{ij}^{\text{nor}} = F_n(\Delta \mathbf{n}_{ij}), \quad \gamma_{ij} = \frac{\exp(s_{ij}^{\text{nor}})}{\sum_{j' \in \mathcal{N}(i)} \exp(s_{ij'}^{\text{nor}})}, \quad (29)$$

where $F_n(\cdot)$ is another two-layer FF network and $\{\gamma_{ij}\}_{j \in \mathcal{N}(i)}$ forms the normal-vector attention branch.

Finally, the near-field edge weight is obtained by combining the two branches, which is compactly expressed as follows:

$$w_{ij} \triangleq \text{MLP}(\beta_{ij} \oplus \gamma_{ij}), \quad (30)$$

where \oplus denotes feature concatenation and $\text{MLP}(\cdot)$ is a multi-layer perceptron. This physics-guided edge attention provides a learnable realization of $\mathcal{G}(\cdot)$ in the near-field formulation, linking local density variation and geometric anisotropy to effective self- and mutual-impedance behavior. The network implementation of the near-field operator in Section II directly follows the iterative message-passing scheme in (8)-(10). Leveraging the graph topology and physics-embedded edge weights w_{ij} established in the construction phase, each iteration realizes the kernel $h_t(\mathbf{w}_{ij}, \mathbf{J}^{(t)}(\mathbf{p}_j))$ using a lightweight stack of attention- and convolution-based graph layers.

The latter approach is sketched in Fig. 4(b). Let $\mathbf{H}^{(0)} = \{\mathbf{J}^{(t)}(\mathbf{p}_i)\}$ denote the initial current features. In particular, the module integrates Graph Attention Networks (GAT) [45]

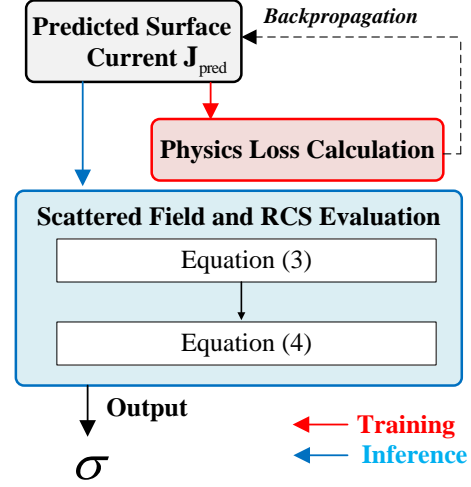


Fig. 5. The proposed physics-driven pipeline. The predicted current \mathbf{J}_{pred} bifurcates into two paths: minimization of the EFIE residual $\mathcal{L}_{\text{phys}}$ for training (red) and evaluation of the RCS $\sigma(\theta, \phi)$ for inference (blue).

and Graph Convolutional Networks (GCN) [46]. One update cycle is implemented as follows:

$$\begin{aligned} \mathbf{H}^{(1)} &\triangleq \text{ELU}\left(\text{BN}\left(\text{GAT}\left(\mathbf{H}^{(0)}, \mathbf{w}\right)\right)\right), \\ \mathbf{H}^{(2)} &\triangleq \text{ELU}\left(\text{BN}\left(\text{GCN}\left(\mathbf{H}^{(1)}, \mathbf{w}\right)\right)\right), \\ \mathbf{H}^{(3)} &\triangleq \text{GCN}\left(\mathbf{H}^{(2)}, \mathbf{w}\right), \\ \mathbf{H}^{(4)} &\triangleq \text{Linear}\left(\mathbf{H}^{(3)}\right). \end{aligned} \quad (31)$$

Here, $\mathbf{H}^{(\ell)}$ are node features at stage ℓ , $\text{GAT}(\cdot, \mathbf{w})$ and $\text{GCN}(\cdot, \mathbf{w})$ are graph attention and graph convolution operators with edge features \mathbf{w} , $\text{BN}(\cdot)$ is batch normalization, $\text{ELU}(\cdot)$ is the exponential linear unit, and $\text{Linear}(\cdot)$ is a trainable affine layer applied node-wise [42]. In this formulation, the first GAT layer uses the physics-guided edge weights w_{ij} 's to modulate directional message passing, providing a learnable counterpart to the anisotropic influence encoded by the near-field MoM interactions. The subsequent GCN layers enforce isotropic neighborhood aggregation, reflecting the smoothing and continuity behavior of \mathbf{Z}_{near} in (10). The final linear map produces the increment $\Delta \mathbf{J}^{(t)}$, which is added to the previous iterate to give the following expression:

$$\mathbf{J}^{(t+1)}(\mathbf{p}_i) = \mathbf{J}^{(t)}(\mathbf{p}_i) + \mathbf{H}_i^{(4)},$$

providing a direct network realization of (8)'s update rule. Repeating this block for T_{iter} iterations yields the near-field output $\mathbf{J}_{\text{near}} = \mathbf{J}^{(T_{\text{iter}})}$, which serves as the finest-level source input to the far-field hierarchy.

B. Hierarchical Far-Field Fusion Module

In the implementation, the operator $\mathbf{\Gamma}_k$ in (15) is realized by an octree-aligned pooling module. At the finest level, the near-field graph module provides the initial source descriptor:

$$\mathbf{S}^{(L)} \leftarrow \mathbf{J}^{T_{\text{iter}}}. \quad (32)$$

For each level $k = L, \dots, 2$, the point set is partitioned into clusters $\{C_c^{(k)}\}$ according to the octree cells, and a coarse-level source representation is obtained by symmetric pooling:

$$\mathbf{S}_c^{(k-1)} = \Gamma_k(\{\mathbf{S}_i^{(k)}\}_{i \in C_c^{(k)}}), \quad (33)$$

where $\mathbf{S}_c^{(k-1)}$ denotes the feature of cluster $C_c^{(k)}$ at level $k-1$ and $\Gamma_k(\cdot)$ is a permutation-invariant pooling operator. This operator is implemented, in practice, combining average and extremal statistics of the points within each cluster. This yields a compact multilevel source hierarchy $\{\mathbf{S}^{(k)}\}_{k=1}^L$ that serves as the input to the subsequent cross-scale translation module.

The global translation operator Φ_k in (16)-(21) is implemented as a shallow transformer-style block. Given the level- k features $\mathbf{S}^{(k)}$ and the unpooled coarse representation $\mathcal{U}_k(\tilde{\mathbf{S}}^{(k-1)})$, we apply a small stack of multi-head cross-attention layers, each followed by a position-wise FF network [43] and residual (with normalization). In practice, this corresponds to a two-stage stack of cross-attention followed by FF refinement, providing a lightweight neural realization of the multilevel translation process in the far-field formulation.

The disaggregation operator Ψ_k in (22) is implemented by a KPCConv-style kernel fusion module that upsamples the coarse-level far-field current and injects the translated source features. At each level k , a set of learnable kernels $\{\mathbf{W}_q^{(k)}\}_{q=1}^{N_{\text{kernel}}}$ acts on $\mathbf{J}_{\text{far}}^{(k-1)}$ through local aggregation, and the result is combined with $\tilde{\mathbf{S}}^{(k)}$ yielding the formulation:

$$\mathbf{J}_{\text{far}}^{(k)} = \tilde{\mathbf{S}}^{(k)} + \sum_{q=1}^{N_{\text{kernel}}} \mathbf{W}_q^{(k)} \mathbf{J}_{\text{far}}^{(k-1)}, \quad (34)$$

where the kernels $\mathbf{W}_q^{(k)}$ are learned from data and play the role of resolution-aware filters on the coarse-level current [47]. Cascading this update from $k = 2$ to L yields the finest-level prediction $\mathbf{J}_{\text{far}} = \mathbf{J}_{\text{far}}^{(L)}$, which serves as the far-field counterpart in the physics-informed loss.

C. Physics-Driven Optimization Mechanism

The final predicted current is obtained by summing the near- and far-field components: $\mathbf{J}_{\text{pred}} = \mathbf{J}_{\text{near}} + \mathbf{J}_{\text{far}}$. Using \mathbf{J}_{pred} , as illustrated in Fig. 5, the EFIE residual $\mathcal{L}_{\text{phys}}$ is evaluated according to the physics-informed residual loss in (24). For a mini-batch of N_s incident fields, the network computes the residual for each sample and averages them to obtain the batch loss as follows:

$$\mathcal{L} = \frac{1}{N_s} \sum_{m=1}^{N_s} \mathcal{L}_{\text{phys}}^{(m)},$$

which drives the end-to-end optimization of all trainable parameters. In this way, U-PINet enforces the boundary condition through batch-level residual minimization, providing a direct neural-network-based realization of the residual evaluation stage in the overall EM reconstruction pipeline.

Finally, using the predicted discrete current \mathbf{J}_{pred} on \mathcal{D} , the scattered electric field and the bistatic RCS are obtained by applying the radiation operator and the far-field definition in expressions (3) and (4), respectively.

TABLE I
TRAINING HYPERPARAMETERS OF U-PINET AND BASELINE MODELS.

Model	Learning Rate	Batch Size	Epochs	Optimizer
ConvNet	Adaptive	32	200	L-M
U-Net	1×10^{-4}	32	200	Adam
MLFMA-PINN	1×10^{-4}	16	100	Adam
U-PINet	5×10^{-4}	64	300	Adam

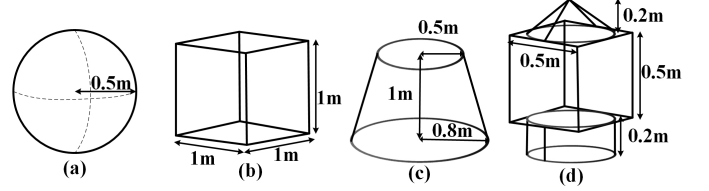


Fig. 6. The considered simple 3D PEC objects for U-PINet's evaluation.

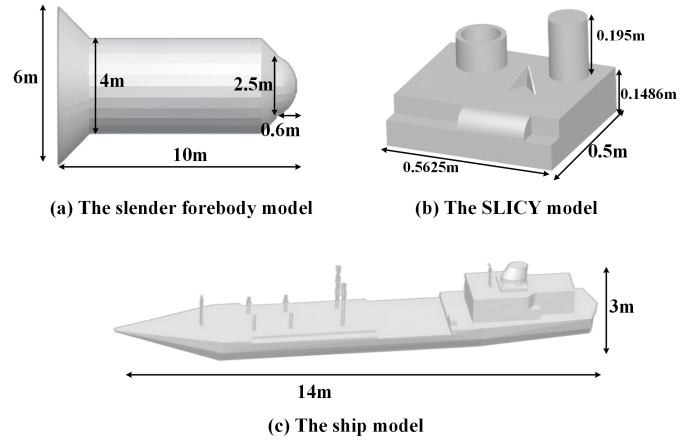


Fig. 7. The complex 3D PEC objects for U-PINet's evaluation.

V. EXPERIMENTAL SETUP

In this section, we introduce the experimental setup to evaluating U-PINet's accuracy considering both simple and complex 3D objects. Fig. 6 shows simple targets with centroids or base centers aligned at the origin, including spheres, conical frustums, and hexahedrons. Complex targets, such as the SLICY model [48] and large-scale objects shown in Fig. 7, exhibit irregular geometries and strong coupling effects. All targets are made of PEC material.

A. Data Generation

We formalize the data pipeline by specifying the inputs, outputs, and ground-truth synthesis, with particular emphasis on the generation and evaluation of RCS. These point clouds, built from the centers of triangular mesh elements and carrying positional information and local EM descriptors, serve as inputs to the U-PINet model. The network outputs the induced surface current on object surfaces, which is used as a physically consistent intermediate representation, and training supervision is provided by MLFMA-computed currents. The scattering setup uses a plane wave with an amplitude of 1 V/m at 1 GHz. Both co-polarized configurations,

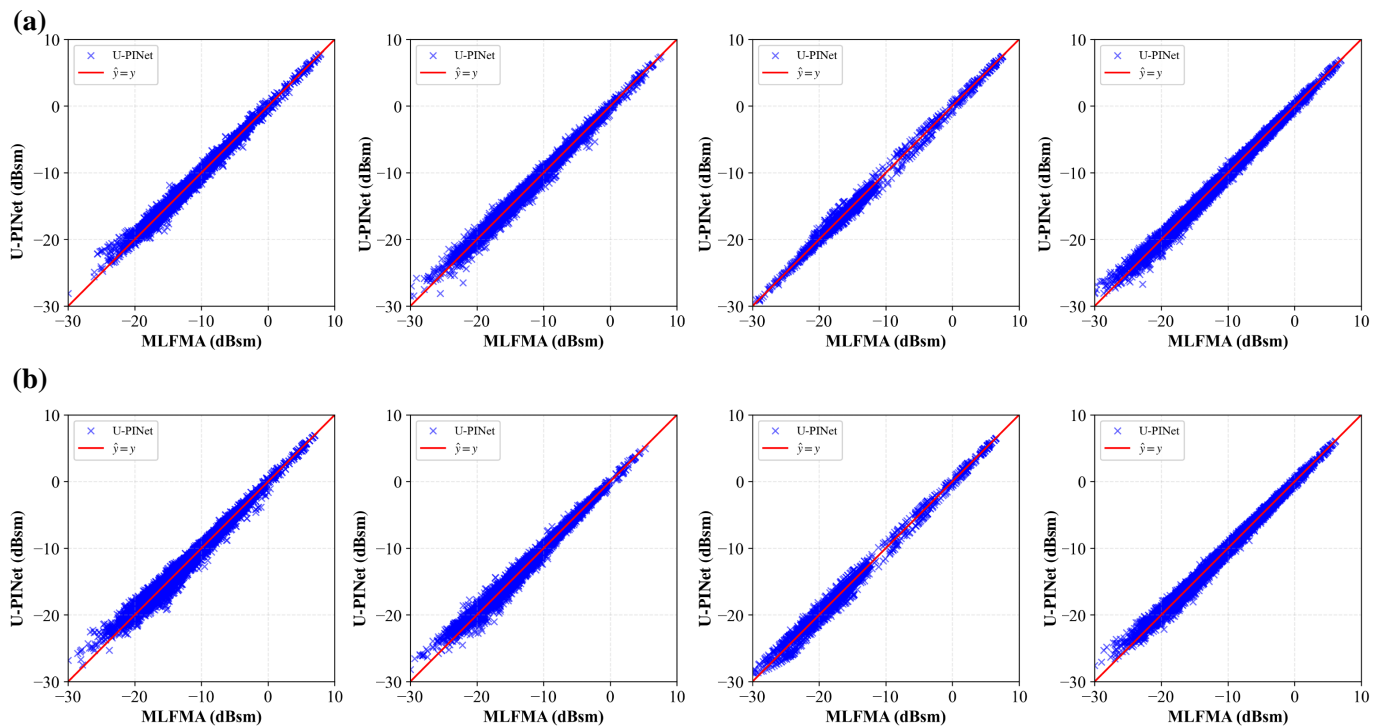


Fig. 8. Regression performance comparison between U-PINet predictions and MLFMA reference values. The rows correspond to (a) HH polarization and (b) VV polarization. The columns, from left to right, represent the sphere, cube, cone, and assembly body targets shown in Fig. 6, respectively. In each scatter plot, the red solid line indicates the ideal identity relationship ($\hat{y} = y$), demonstrating the agreement between the predicted and reference results.

namely horizontal–horizontal (HH) and vertical–vertical (VV), are considered for each target to account for polarization-dependent RCS behavior. Observation angles are sampled over $\theta \in [0^\circ, 180^\circ]$ and $\phi \in [0^\circ, 180^\circ]$. For each object and incidence, surface-current ground truth is generated with the MLFMA under varying incident angles, polarizations, and geometries. The initial triangular meshes use an average edge length of $\lambda/10$; for highly complex shapes, we relax to $\lambda/5$ to keep the number of elements tractable. To further assess physical fidelity, RCS is computed from both the predicted and reference currents via the radar equation (4) on the same observation grid, and the two are compared.

B. Benchmark Models and Evaluation Metrics

Three representative baseline models for EM scattering reconstruction, including two mainstream data-driven deep learning methods and one physics-informed hybrid model, have been implemented and compared.

- **ConvNet** [21]: This approach applies a fully CNN to predict potential distributions in 3D EM models. The architecture consists of seven convolutional layers with Rectified Linear Unit (ReLU) activations and no pooling layers, designed to preserve local detail and maintain numerical accuracy.
- **U-Net** [22]: This method employs a physics-augmented U-Net architecture for EM-field prediction, consisting of an encoder-decoder structure with six residual blocks. Each block includes six convolutional layers, followed by batch normalization and leaky ReLU activations. Physics

loss terms derived from Maxwell’s equations are incorporated during training to enhance physical consistency.

- **MLFMA-PINN** [36]: This model replaces the analytical computation of the translation operators in MLFMA with a hybrid Generalized Regression Neural Network (GRNN) and Artificial Neural Network (ANN) framework. ANN handles coarse-level translations through a 12-layer fully connected network with descending neuron sizes and $\tanh(\cdot)$ activations, while GRNN is used at fine levels for nonlinear regression with a Gaussian kernel.

By benchmarking **U-PINet** against the end-to-end baselines and the solver-guided MLFMA-PINN, we aim to compare the ability of all models to achieve prediction accuracy comparable to classical MLFMA solutions and substantially reduce computational complexity. We adopt MLFMA-PINN as a representative hybrid approach.

To comprehensively evaluate the reconstruction accuracy and scattering consistency of the proposed framework, five physically interpretable error metrics are employed. Specifically, the Root-Mean-Square Error (RMSE), Absolute Error (AE), Mean Absolute Error (MAE), Mean Absolute Percentage Error (MAPE), and the Coefficient of Determination (R^2) are adopted to quantify the prediction performance for both the induced surface current and the far-field RCS responses [49].

Unless otherwise stated, all reported metrics in Section VI are computed with respect to the MLFMA-based reference solutions, i.e., by comparing each model’s predicted currents/RCS against the corresponding MLFMA ground truth under the same geometry and excitation/observation settings.

TABLE II
OVERALL RCS REGRESSION PERFORMANCE (RMSE, R^2 , MAE, AND MAPE) OF ALL COMPARED METHODS ON SIMPLE AND COMPLEX 3D PEC TARGETS.

Target	ConvNet				U-Net				MLFMA-PINN				U-PINet (Proposed)			
	RMSE↓	R^2 ↑	MAE↓	MAPE↓	RMSE↓	R^2 ↑	MAE↓	MAPE↓	RMSE↓	R^2 ↑	MAE↓	MAPE↓	RMSE↓	R^2 ↑	MAE↓	MAPE↓
Cube	1.1542	0.8520	0.9231	0.1245	0.9854	0.9102	0.8124	0.0923	0.7921	0.9785	0.6352	0.0654	0.7685	0.9815	0.6120	0.0452
Sphere	0.9823	0.8845	0.8125	0.1020	0.8452	0.9250	0.7102	0.0854	0.6754	0.9820	0.5421	0.0521	0.6542	0.9850	0.5215	0.0385
Cone	1.2540	0.8410	1.0542	0.1314	1.0821	0.8954	0.9210	0.0954	0.8354	0.9712	0.6954	0.0685	0.8120	0.9750	0.6752	0.0510
Assembly body	1.3852	0.8320	1.1520	0.1454	1.1542	0.8850	0.9852	0.1045	0.9152	0.9654	0.7521	0.0720	0.8897	0.9704	0.7254	0.0585
SLICY	2.4542	0.8250	2.0420	0.2854	2.1521	0.8650	1.7540	0.2251	1.6520	0.9585	1.4521	0.1454	1.5640	0.9620	1.3520	0.1250
Slender forebody	3.4520	0.7250	2.9520	0.4120	2.9520	0.7820	2.4520	0.3654	2.2054	0.9350	1.9852	0.1852	2.1540	0.9410	1.9520	0.1580
Ship	4.1540	0.6520	3.5520	0.4840	3.6520	0.7150	3.0520	0.4254	2.7120	0.8885	2.3520	0.2054	2.6540	0.8950	2.2850	0.1750

Note: ↓ indicates lower is better and ↑ indicates higher is better. Best results are highlighted in bold.

C. Training Configuration

To ensure fair comparisons, all the models are trained under a unified data partitioning scheme, with an 80 : 20 split between training and test sets. The input data were uniformly preprocessed into point cloud representations with aligned EM attributes, ensuring consistency across methods. A summary of the key configurations (network architectures and training hyperparameters) of all three baseline models and U-PINet is provided in Table I. The U-PINet is trained for 300 epochs with an initial learning rate of 5×10^{-4} . For the baseline models, their original settings for the optimizer and training strategy were used. All models are implemented in PyTorch 2.1 and trained on a single NVIDIA RTX 3090Ti GPU.

VI. EXPERIMENTAL RESULTS AND DISCUSSION

In this section, we present 3D object reconstruction results with the proposed U-PINet model and compare them with baselines, using the experimental setup settings detailed in the previous Section V.

A. Feasibility Verification

Fig. 8 visualizes the regression performance on simple targets. The scatter points for both HH and VV polarizations tightly cluster along the diagonal $\hat{y} = y$ line, demonstrating high predictive fidelity. This visual alignment is quantitatively corroborated by Table II, where U-PINet achieves an R^2 exceeding 0.97 and an RMSE below 0.9 dBm for all simple 3D PEC objects (Fig. 6), confirming the model’s robustness across different polarization states.

Table II summarizes the RMSE, R^2 , MAE, and MAPE metrics for all compared methods on both simple 3D PEC objects (Fig. 6) and complex 3D PEC objects (Fig. 7). Overall, the proposed method achieves at least 27% and 12% improvement over the comparison methods in terms of RMSE and R^2 , respectively, demonstrating its superior ability to learn the distribution of RCS across different numerical ranges and to achieve more accurate fitting performance. In addition, improvements of at least 18% and 20% are obtained in MAE and MAPE, respectively, indicating fewer outliers during continuous prediction, smaller overall estimation errors, and more stable predictive performance.

Furthermore, Fig. 9 illustrates the RCS prediction results for the SLICY target shown in Fig. 7(a) under continuously

varying observation angles. In this experiment, the elevation angle θ is fixed at 30° , 70° , 120° , and 150° , while the azimuth angle ϕ varies continuously from 0° to 180° . It can be observed that the predictions of U-PINet (red curves) closely match those of MLFMA-PINN (gray curves) and the reference results (blue curves). Notably, the sharp edges and corners of the SLICY geometry induce pronounced edge diffraction effects, which introduce stronger nonlinearity and angle sensitivity into the scattering responses. In such cases, purely data-driven models (ConvNet and U-Net) often struggle to stably capture the underlying EM mechanisms, whereas physics-guided approaches such as U-PINet and MLFMA-PINN demonstrate superior representation and learning capabilities.

For more complex targets, the RCS exhibits more pronounced fluctuations with respect to the observation angles, primarily due to increased geometric complexity and stronger nonlinear mutual coupling effects. For the slender forebody model in Fig. 7(b) and the ship target in Fig. 7(c), dynamic RCS sequences are generated over $\theta \in [0^\circ, 90^\circ]$ and $\phi \in [0^\circ, 180^\circ]$, and are arranged in ascending order of θ and ϕ . Figures 10 and 11 present the two-dimensional heatmaps of the RCS predictions produced by U-PINet, where panels (a) and (b) correspond to HH and VV polarizations, respectively. It can be seen that the RCS predictions of U-PINet closely follow the MLFMA reference results, and the residuals remain relatively uniformly distributed under continuous angle variations, indicating good stability and consistency.

These results collectively demonstrate that U-PINet effectively encodes and preserves EM priors. It exhibits both structural fidelity and predictive accuracy, laying a solid foundation for its use as a general-purpose, PINN-based framework for EM scattering reconstruction. This positions U-PINet not merely as a surrogate model, but as a physically-grounded emulator capable of replacing classical solvers.

B. Accuracy and Generalization Results

1) *Induced-Current Reconstruction Accuracy*: We first assess the reconstruction accuracy at the level of the fundamental induced surface current density \mathbf{J} . This evaluation is essential because the far-field scattered response and the resulting RCS signatures are not directly regressed by the proposed network, but are instead obtained by applying the radiation operator to

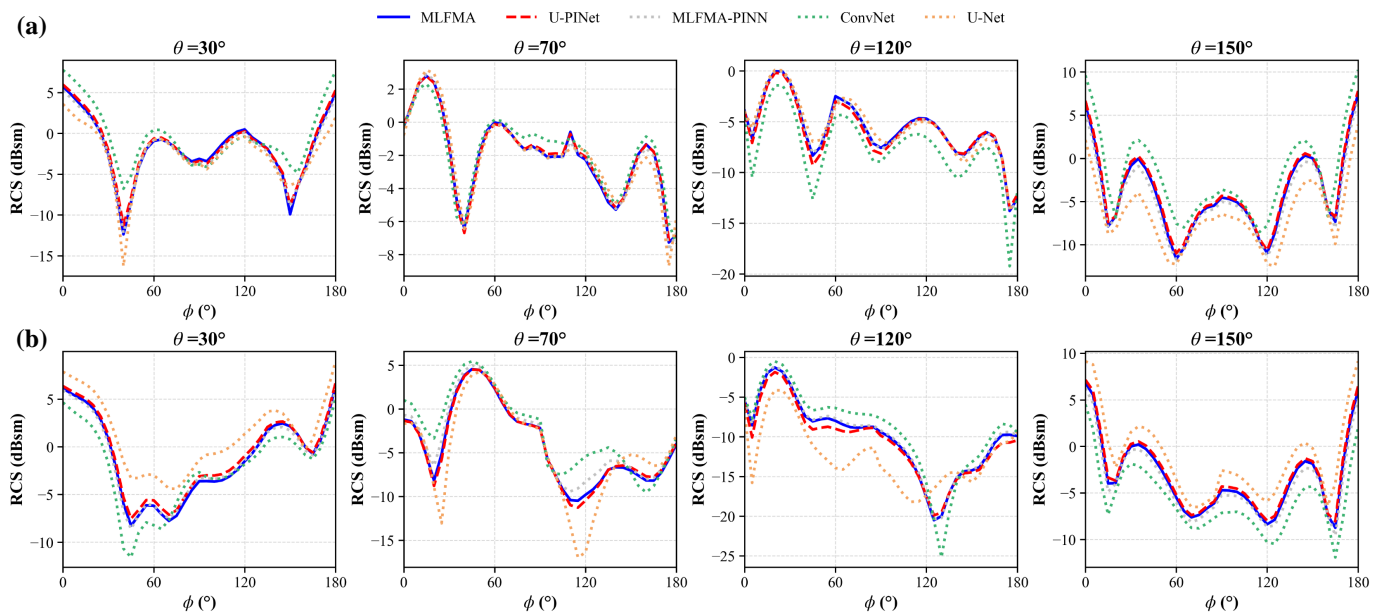


Fig. 9. Comparison of RCS reconstruction performance on the SLICY target (Fig. 7(b)). The curves illustrate the RCS values with the azimuth angle ϕ varying continuously from 0° to 180° at fixed elevation angles of $\theta = 30^\circ, 70^\circ, 120^\circ$, and 150° (from left to right). The results are presented for (a) HH polarization and (b) VV polarization.

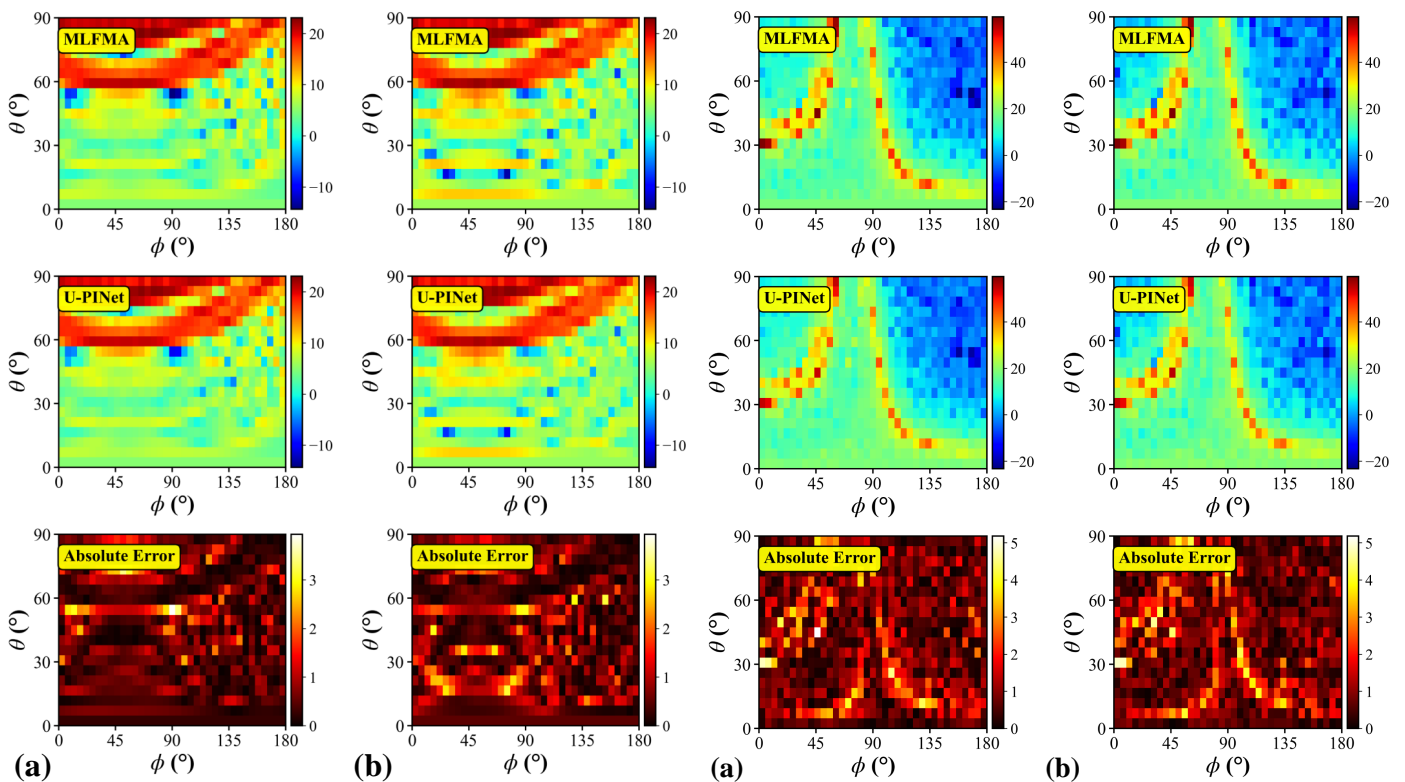


Fig. 10. Visual comparison and residual analysis of RCS predictions for the slender forebody (Fig. 7(a)) across the angular domain of $\theta \in [0^\circ, 90^\circ]$ and $\phi \in [0^\circ, 180^\circ]$. The heatmaps depict MLFMA (top), U-PINet (middle), and absolute error (bottom) for (a) HH and (b) VV polarizations.

the reconstructed currents. Therefore, accurate reconstruction of \mathbf{J} serves as the primary indicator of physically consistent EM scattering reconstruction and directly determines the fidelity of the downstream RCS prediction.

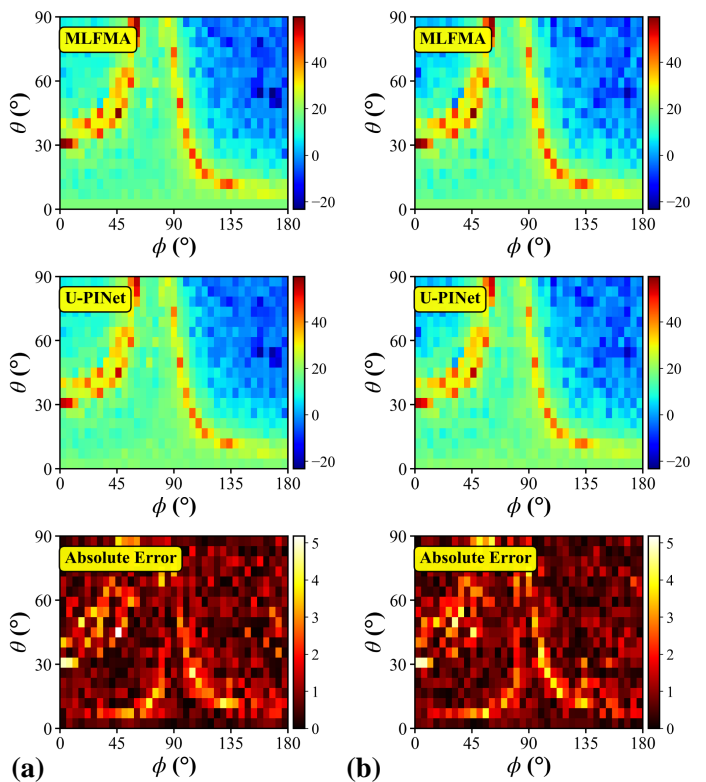


Fig. 11. Visual comparison and residual analysis of RCS predictions for the ship (Fig. 7(c)) across the angular domain of $\theta \in [0^\circ, 90^\circ]$ and $\phi \in [0^\circ, 180^\circ]$. The heatmaps depict MLFMA (top), U-PINet (middle), and absolute error (bottom) for (a) HH and (b) VV polarizations.

As a foundational validation step, we examine the network's performance on the three canonical targets (cube, sphere, and cone) shown in Fig. 6. Fig. 12 shows a strong qualitative agreement between the reconstructed induced currents and

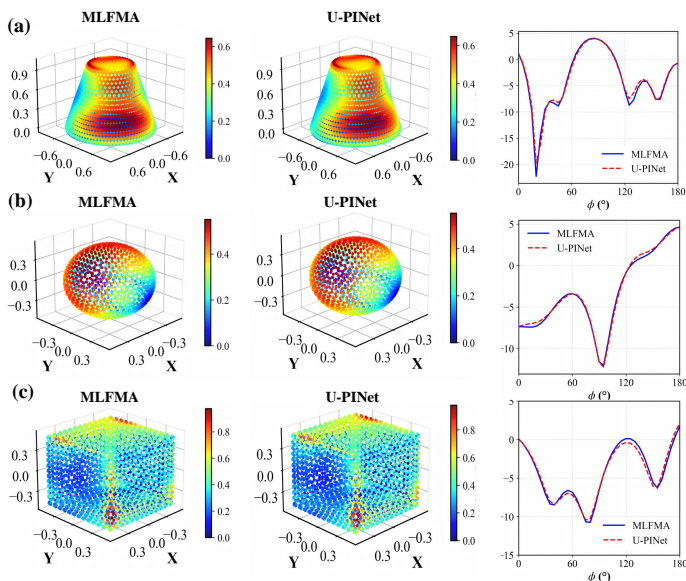


Fig. 12. Visualization of induced surface currents and resultant RCS predictions for (a) the cone, (b) the sphere, and (c) the cube defined in Fig. 6. The columns display the MLFMA ground truth (left), U-PINet predictions (middle), and the derived HH-polarized RCS curves (right).

the MLFMA solutions, with highly consistent spatial structures. This fidelity is quantitatively corroborated by negligible error metrics: the MSEs for all three cases are consistently constrained below 8.0×10^{-4} (with average 6.5×10^{-4}), while the MAPEs stabilize around 1.9% \sim 2.5%. These results establish a solid baseline, confirming that U-PINet can perfectly encode the fundamental scattering mechanisms on standard geometries.

Moving to complex geometries, Fig. 13 visualizes the predicted current distributions for (a) the assembly body and (b) the slender forebody model. For the former, the main difficulty stems from pronounced EM coupling among its composite components, which results in localized interaction hot-spots and rapidly varying current structures near coupled regions. Despite this complexity, it is depicted that the predicted currents preserve the dominant spatial patterns, quantitatively achieving a MSE of 2.14×10^{-3} and a MAPE of 5.36%. These metrics indicate that the proposed near-far hierarchical network can effectively capture both local coupling and global radiation-consistent behavior, which aligns well with the low far-field RCS error. For the slender forebody, U-PINet similarly reconstructs physically plausible current flows over complex geometric regions, including transition zones and boundary contours, where high gradients typically challenge learning-based solvers. Specifically, it is demonstrated that the proposed network maintains an MSE of 4.85×10^{-3} and a MAPE of 9.20% across the testing set. While slightly higher than that of the assembly body due to the slender geometry’s sensitivity to edge diffraction, the predicted distributions remain highly consistent with the MLFMA reference.

Finally, to evaluate robustness under varying excitation conditions, we consider the SLICY target (from Fig. 7(b)) and reconstruct the induced currents under multiple incident directions $(\theta_{\text{inc}}, \phi_{\text{inc}})$, as illustrated in Fig. 14. This experi-

ment keeps the geometry fixed while changing the incident angle, thereby directly testing whether the model captures the illumination-dependent scattering response. Due to its sharp edges and corner-reflector structures, SLICY exhibits pronounced edge diffraction and localized scattering singularities. As shown in Fig. 14, U-PINet closely follows these incidence-driven redistributions of the current patterns and maintains strong agreement with the MLFMA reference across the tested angles. Quantitatively, the reconstruction accuracy on SLICY achieves an MSE of 3.25×10^{-3} and a MAPE of 7.82%. These results indicate that U-PINet learns a generalized geometry–excitation–current mapping, rather than overfitting to a single incident configuration, and thus supports consistent downstream RCS evaluation via the same physics closure.

Collectively, these results substantiate that U-PINet achieves accurate RCS prediction via 3D EM scattering reconstruction by reconstructing the physically meaningful induced currents and subsequently evaluating the scattered fields and RCS through the governing radiation formulation.

2) *Generalization*: To evaluate the generalization capability of U-PINet on unseen geometries, a leave-one-geometry strategy is adopted. The model is pre-trained on canonical targets and adapted to two structurally distinct and more complex geometries, namely the SLICY and slender forebody models in Fig. 7, using only 80%, 20%, and 10% of the downstream datasets. Figure 15 reports the resulting RCS error CDFs and bistatic RCS curves, where panels (a) and (b) correspond to HH and VV polarizations, respectively, and the left and right columns represent the SLICY and slender forebody targets.

Under HH polarization, the 1.0 dB CDF for the SLICY target decreases from 0.70 (80%) to 0.62 (20%) and 0.55 (10%), while the 2.0 dB CDF remains high at 0.95, 0.92, and 0.88; for the slender forebody, the corresponding values decrease from 0.58 to 0.47 and 0.42 at 1.0 dB, and remain at 0.91, 0.83, and 0.76 at 2.0 dB. Similar trends are observed under VV polarization, where the SLICY model shows 1.0 dB CDF values of 0.72, 0.64, and 0.56, and 2.0 dB CDF values of 0.96, 0.91, and 0.89, while the slender forebody yields 1.0 dB CDF values of 0.61, 0.51, and 0.46, and 2.0 dB CDF values of 0.89, 0.81, and 0.77.

Overall, these results demonstrate that U-PINet preserves most of its RCS prediction accuracy under severely limited adaptation data, indicating strong generalization capability across both polarizations and complex geometries.

C. 3D Object Reconstruction Time Results

Table III summarizes the reconstruction time in seconds of Fig. 6’s cube, sphere, and cone objects, as well as Fig. 7’s SLICY and ship targets, using the U-PINet, the conventional EM scattering reconstruction approaches MoM and MLFMA, as well as MLFMA-PINN and ConvNet. It can be observed that the U-PINet achieves a substantial speed of computation advantage over physics-based solvers, reducing runtime reductions of several orders of magnitude across both canonical (cube, sphere, and cone) and complex (SLICY and ship) 3D geometries. For example, the U-PINet completes inference on the ship model in only 0.12 seconds, whereas the MoM

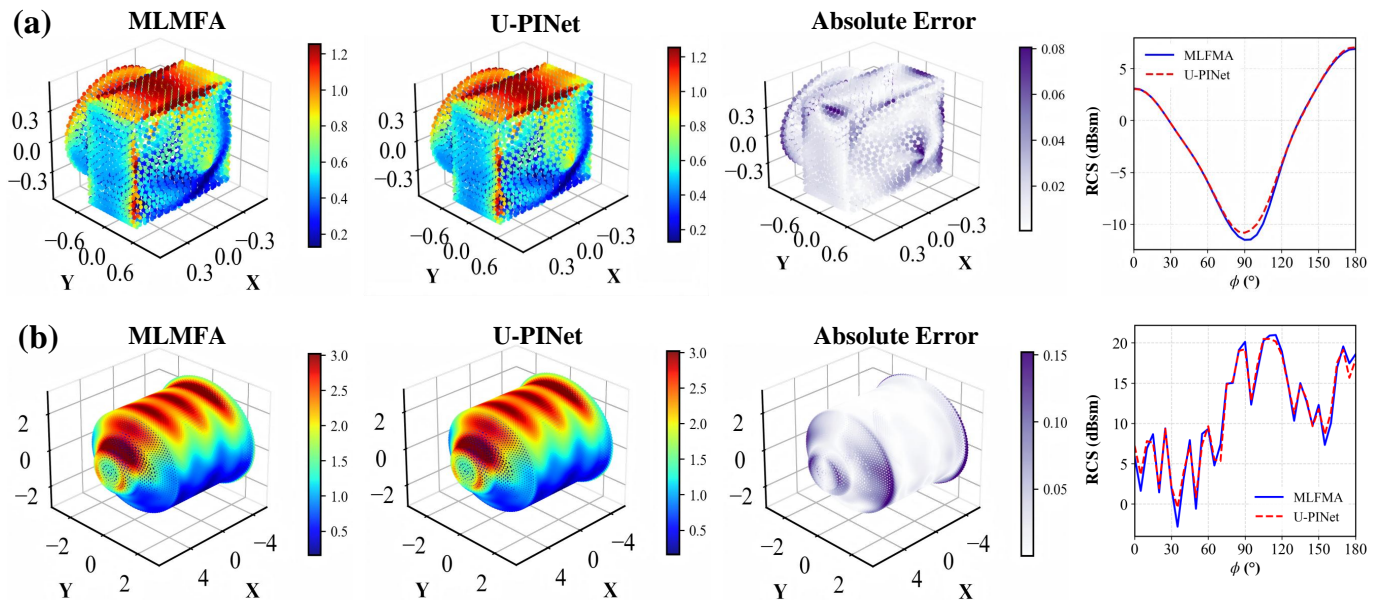


Fig. 13. Visualization of induced surface currents and resultant RCS predictions. The rows correspond to (a) the assembly body (Fig. 6(d)) and (b) the slender forebody (Fig. 7(a)). From left to right, the columns illustrate the current distribution computed by MLMFA, the U-PINet prediction, the absolute error map, and the HH-polarized RCS curves derived from these currents.

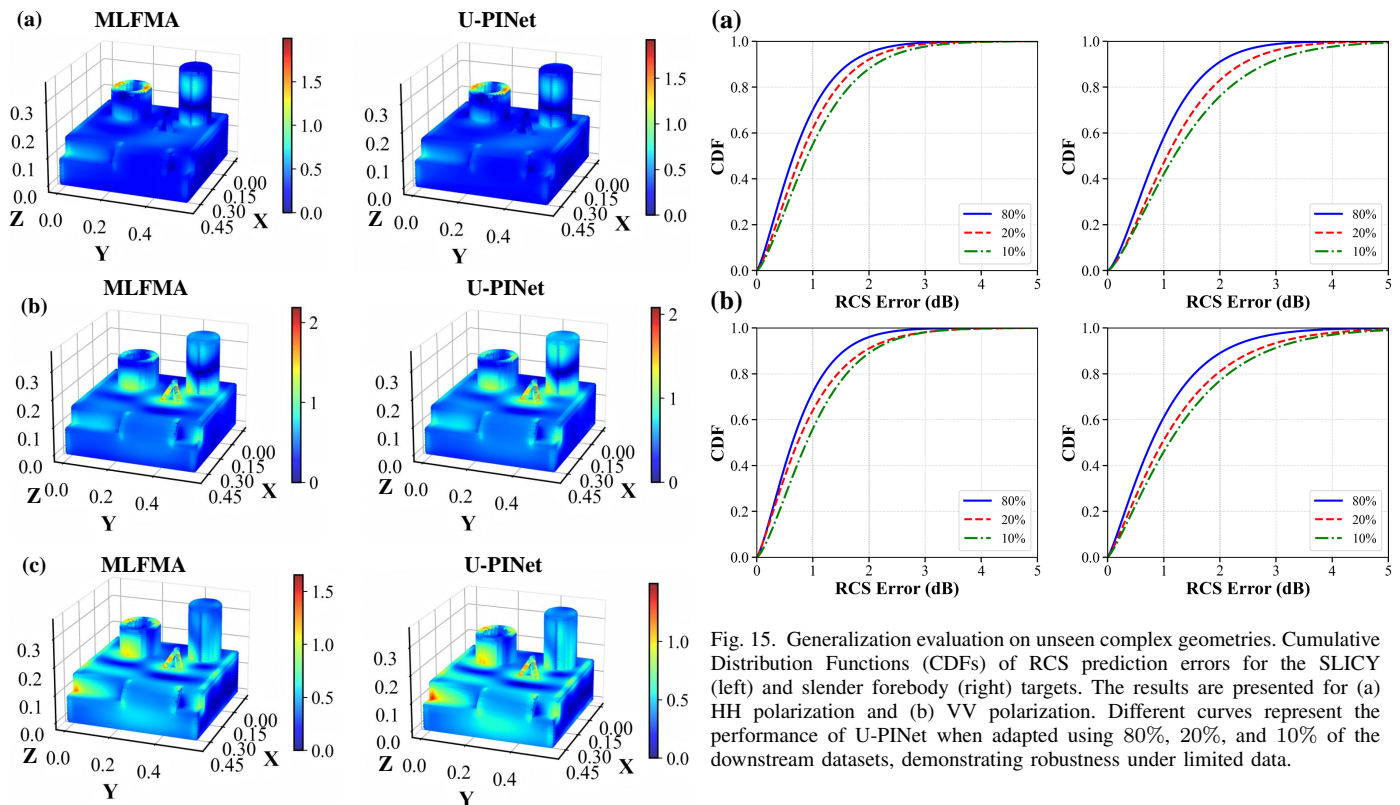


Fig. 14. Surface current magnitude distributions computed by MLMFA (left column) and U-PINet (right column) for the SLICY target under different incident angles. Rows (a), (b), and (c) correspond to distinct elevation angles $\theta_{\text{inc}} = 0^\circ, 45^\circ,$ and 90° , respectively, at the fixed azimuth angle $\phi_{\text{inc}} = 0^\circ$.

requires over 80000 seconds for the same task. Compared to the MLMFA-PINN, the U-PINet reduces runtime by up to three orders of magnitude, while preserving competitive

accuracy. It is finally shown that the ConvNet runs slightly faster than the proposed model, however, ConvNet's error rates and instability under geometric variation makes it unsuitable for practical EM applications. Concluding, the results in this table underscore U-PINet's capability as a fast and reliable surrogate model for EM simulations.

TABLE III
RECONSTRUCTION TIME WITH U-PINET AND BASELINE SCHEMES
FOR FOUR DIFFERENT 3D OBJECTS.

Time (sec)	Cube	Sphere	Cone	SLICY	Ship
MoM	260.3	253.8	264.2	112.9	80188.9
MLFMA	240.5	212.3	221.1	103.2	62156.9
U-PINet	0.05	0.04	0.03	0.03	0.12
MLFMA-PINN	10.05	7.54	9.73	6.23	300.42
ConvNet	0.01	0.01	0.01	0.01	0.03

TABLE IV
ABLATION STUDY ON THE RCS RECONSTRUCTION PERFORMANCE OF
U-PINET FOR THE SHIP TARGET IN FIG. 7(C).

Setting	RMSE	R^2	MAE	MAPE
Without physics loss	3.4520	0.7540	2.9540	0.3850
Without edge attention	2.9250	0.8420	2.5120	0.2450
U-PINet (full)	2.6540	0.8950	2.2850	0.1750

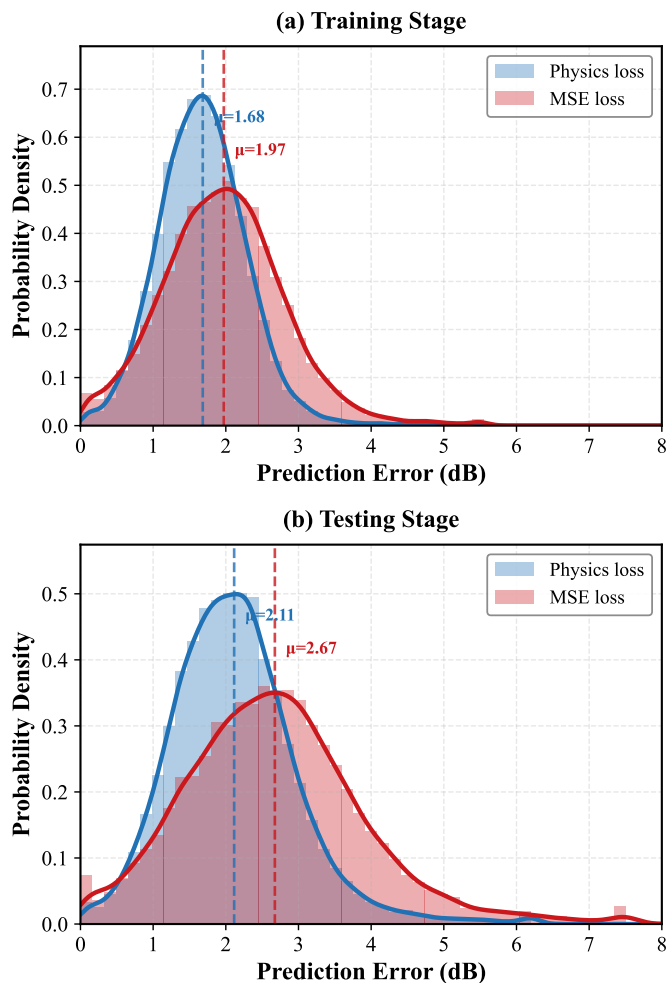


Fig. 16. Reconstruction error distribution with U-PINet when using the loss function in (24) (with physics constraints) and an MSE-based loss function (without physics constraints) in the process of inducing current in Fig. 7(a)’s slender forebody model during training. Dashed lines indicate kernel density estimates over the histogram distributions.

D. Ablation Capability

We further investigate the effect of the physics-informed residual loss on the error distribution of U-PINet during the current induction process. The reconstruction error distributions under the physics-informed loss in (24) and the purely data-driven MSE loss are compared for both the training and testing stages on the slender forebody model in Fig. 7 (a), as shown in Fig. 16.

For the training stage, the physics-constrained loss yields a noticeably more compact distribution, with the mean error reduced from $\mu = 1.85$ dB (MSE loss) to $\mu = 1.62$ dB and a visibly suppressed right tail. In contrast, the MSE-based training distribution exhibits a broader spread and heavier tail, indicating weaker control over large-error samples. Similar behavior is observed in the testing stage, where the mean error under the physics loss is reduced from $\mu = 2.35$ dB (MSE loss) to $\mu = 1.95$ dB, together with a significantly lower probability mass in the high-error region.

To quantify the contributions of the physics-aware and interpretable modules in U-PINet, an ablation study is conducted on the complex ship target shown in Fig. 7(c). The quantitative results, evaluated using the four reconstruction metrics in Section V-B, are summarized in Table IV. Specifically, the full U-PINet is compared with two degraded variants, namely, a model without the physics-informed loss in (24) and another with the edge attention module removed. As shown in Table IV, removing either component consistently degrades the regression performance.

Specifically, when the physics-informed loss is excluded, the model reverts to a purely data-driven approach, causing the RMSE to deteriorate significantly from 2.65 dB to 3.45 dB, while the MAE increases from 2.29 dB to 2.95 dB. This substantial performance drop underscores the critical role of physical constraints in regularizing the solution space and mitigating overfitting on limited data. Similarly, removing the edge attention module results in a noticeable accuracy loss, with the RMSE rising to 2.93 dB and the MAPE increasing from 0.1750 to 0.2450. This degradation confirms that the attention mechanism is essential for capturing high-frequency scattering features localized at sharp geometric edges, which are dominant in the RCS of complex targets like the ship. Ultimately, the full U-PINet achieves the lowest errors and the highest correlation ($R^2 = 0.8950$), demonstrating that the synergistic integration of physical laws and attention-based feature extraction is key to high-fidelity RCS prediction. These results indicate that the physics-informed loss primarily enforces global physical consistency suppressing large scattering errors, while the edge attention module refines local behavior around geometric discontinuities. Their combination is therefore essential for achieving the full U-PINet performance.

VII. CONCLUSION AND FUTURE DIRECTIONS

In this paper, we propose U-PINet, an end-to-end physics-informed framework for efficient RCS prediction via 3D EM scattering reconstruction. The proposed artificial neural

network reconstructs the fundamental scattering quantity of the induced surface currents, and then evaluates the scattered field and RCS through the radiation integral and far-field definition, rather than directly regressing RCS. By combining a physics-guided near-field graph module for local coupling with a hierarchical far-field module for long-range radiation, U-PINet attains solver-level RCS accuracy on both canonical and complex targets with orders of magnitude runtime reduction, while generalizing well to unseen geometries and varying observation conditions under limited training data.

Future work will focus on extending U-PINet to broadband RCS analysis and incorporating mechanism-based architectures, such as Kolmogorov-Arnold networks [50], to further enhance interpretability. Additionally, we aim to apply the framework to downstream radar signal processing tasks, including synthetic aperture radar (SAR) imaging and automatic target recognition, where the rapid generation of high-fidelity scattering signatures is critical.

REFERENCES

- [1] A. D. De Quevedo, F. I. Urzaiz, J. G. Menoyo, and A. A. López, "Drone detection and RCS measurements with ubiquitous radar," in *2018 Int. Conf. Radar (RADAR)*, 2018, pp. 1–6.
- [2] K. El-Darymli, E. W. Gill, P. McGuire, D. Power *et al.*, "Automatic target recognition in synthetic aperture radar imagery: A state-of-the-art review," *IEEE Access*, vol. 4, pp. 6014–6058, 2016.
- [3] A. Hanif, M. Muaz, A. Hasan, and M. Adeel, "Micro-Doppler based target recognition with radars: A review," *IEEE Sensors J.*, vol. 22, no. 4, pp. 2948–2961, 2022.
- [4] C. A. Balanis, *Advanced Engineering Electromagnetics*, 2nd ed. Hoboken, NJ, USA: Wiley, 2012.
- [5] E. F. Knott, J. F. Schaeffer, and M. T. Tuley, *Radar Cross Section*, 2nd ed. Dedham, MA, USA: Artech House, 1993.
- [6] R. F. Harrington, *Field Computation by Moment Methods*. Oxford, U.K.: Oxford Univ. Press, 1996.
- [7] J.-M. Jin, *The Finite Element Method in Electromagnetics*. Hoboken, NJ, USA: Wiley, 2015.
- [8] A. Taflove, S. C. Hagness, and M. Picket-May, "Computational electromagnetics: The finite-difference time-domain method," in *The Electrical Engineering Handbook*, 3rd ed. Boca Raton, FL, USA: CRC Press, Jan. 2005, pp. 629–670.
- [9] D. Poljak, *Advanced Modeling in Computational Electromagnetic Compatibility*. Hoboken, NJ, USA: Wiley, 2007.
- [10] V. V. S. Prakash and R. Mitra, "Characteristic basis function method: A new technique for efficient solution of method of moments matrix equations," *Microw. Opt. Technol. Lett.*, vol. 36, no. 2, pp. 95–100, Jan. 2003.
- [11] G.-Y. Zhu, W.-D. Li, W. E. I. Sha, H.-X. Zhou *et al.*, "A directional multilevel complex-space fast multipole algorithm for electrically large problems of various dimensions," *IEEE Trans. Antennas Propag.*, vol. 72, no. 1, pp. 22–36, Jan. 2024.
- [12] A. Noga, T. Topa, and A. Karwowski, "Using GPU accelerated version of MoM for solving scattering and radiation electromagnetic problems," in *Proc. 19th Int. Conf. Microw., Radar Wireless Commun. (MIKON)*, Warsaw, Poland, 2012, pp. 233–234.
- [13] W.-J. He, Z. Yang, X.-W. Huang, W. Wang, and others., "Solving electromagnetic scattering problems with tens of billions of unknowns using GPU accelerated massively parallel MLFMA," *IEEE Trans. Antennas Propag.*, vol. 70, no. 7, pp. 5672–5682, Jul. 2022.
- [14] J. Song, C.-C. Lu, and W. C. Chew, "Multilevel fast multipole algorithm for electromagnetic scattering by large complex objects," *IEEE Trans. Antennas Propag.*, vol. 45, no. 10, pp. 1488–1493, Oct. 1997.
- [15] Y.-N. Liu and X.-M. Pan, "Solution of volume–surface integral equation accelerated by MLFMA and skeletonization," *IEEE Trans. Antennas Propag.*, vol. 70, no. 7, pp. 6078–6083, Jul. 2022.
- [16] C. Wu, L. Guan, P. Gu, and R. Chen, "Application of parallel CM-MLFMA method to the analysis of array structures," *IEEE Trans. Antennas Propag.*, vol. 69, no. 9, pp. 6116–6121, Sep. 2021.
- [17] M. Takrimi, Ö. Ergül, and V. B. Ertürk, "A broadband multilevel fast multipole algorithm with incomplete-leaf tree structures for multiscale electromagnetic problems," in *Proc. 10th Eur. Conf. Antennas Propag. (EuCAP)*, 2016.
- [18] R. Guo, X. Song, M. Li, F. Yang, and others., "Supervised descent learning technique for 2-D microwave imaging," *IEEE Trans. Antennas Propag.*, vol. 67, no. 5, pp. 3550–3554, May 2019.
- [19] T. Shan, R. Guo, M. Li, F. Yang, and others., "Application of multitask learning for 2-D modeling of magnetotelluric surveys: TE case," *IEEE Trans. Geosci. Remote Sens.*, vol. 60, pp. 1–9, 2022.
- [20] J. H. Kim and S. W. Choi, "A deep learning-based approach for radiation pattern synthesis of an array antenna," *IEEE Access*, vol. 8, pp. 226059–226063, 2020.
- [21] T. Shan *et al.*, "Study on a fast solver for Poisson's equation based on deep learning technique," *IEEE Trans. Antennas Propag.*, vol. 68, no. 9, pp. 6725–6733, Sep. 2020.
- [22] M. Chen, R. Lupoïu, C. Mao *et al.*, "WaveY-Net: Physics-augmented deep learning for high-speed electromagnetic simulation and optimization," in *Proc. SPIE High Contrast Metastructures XI*, vol. 12011, 2022, pp. 63–66.
- [23] H. Shin, J. K. Lee, J. Kim, and J. Kim, "Continual learning with deep generative replay," in *Proc. 31st Int. Conf. Neural Inf. Process. Syst. (NeurIPS)*, Long Beach, CA, USA, 2017, pp. 2994–3003.
- [24] K. Chai, H. Zeng, A. Li, and E. W. T. Ngai, "Deep learning in computer vision: A critical review of emerging techniques and application scenarios," *Mach. Learn. Appl.*, vol. 6, p. 100134, 2021.
- [25] M. Baldan, P. Di Barba, and D. A. Lowther, "Physics-informed neural networks for inverse electromagnetic problems," *IEEE Trans. Magn.*, vol. 59, no. 5, pp. 1–5, May 2023.
- [26] C. Brennan and K. McGuinness, "Site-specific deep learning path loss models based on the Method of Moments," in *Proc. 17th Eur. Conf. Antennas Propag. (EuCAP)*, Florence, Italy, 2023, pp. 1–5.
- [27] W.-J. He, X.-W. Huang, M.-L. Yang, and X.-Q. Sheng, "Massively parallel multilevel fast multipole algorithm for extremely large-scale electromagnetic simulations: A review," *Prog. Electromagn. Res.*, vol. 173, pp. 37–52, 2022.
- [28] Y. Liu, H. Zhao, R. Song, X. Chen, and others., "SOM-Net: Unrolling the subspace-based optimization for solving full-wave inverse scattering problems," *IEEE Trans. Geosci. Remote Sens.*, vol. 60, pp. 1–15, 2022.
- [29] L. Zhang *et al.*, "A deep generative model-integrated framework for 3-D time-difference electrical impedance tomography," *IEEE Trans. Instrum. Meas.*, vol. 72, pp. 1–12, 2023.
- [30] X. Xue, L. Lei, S. Sun, J. Hu, and others., "Electromagnetic modeling of numerical Green's function for moving scatterers using artificial neural networks," in *Proc. 2023 Int. Appl. Comput. Electromagn. Soc. Symp. (ACES-China)*, Hangzhou, China, 2023, pp. 1–2.
- [31] R. Guo *et al.*, "Physics embedded deep neural network for solving volume integral equation: 2-D case," *IEEE Trans. Antennas Propag.*, vol. 70, no. 8, pp. 6135–6147, Aug. 2022.
- [32] K. Stylianopoulos, P. N. Gavriilidis, G. Gradoni, and G. C. Alexandropoulos, "Graph-CNNs for RF imaging: Learning the electric field integral equations," in *Proc. 33rd Eur. Signal Process. Conf. (EUSIPCO)*, 2025, pp. 905–909.
- [33] S. Shan, M. Li, F. Yang, and S. Xu, "Solving combined field integral equations with physics-informed graph residual learning for EM scattering of 3-D PEC targets," *IEEE Trans. Antennas Propag.*, vol. 72, no. 1, pp. 733–744, Jan. 2024.
- [34] W. Wan, P. Hou, and X. Pu, "Optimizing translation operator calculation in MLFMA based on neural network integration," in *Proc. 2024 IEEE MTT-S Int. Microw. Workshop Ser. Adv. Mater. Process. RF THz Appl. (IMWS-AMP)*, Nanjing, China, 2024, pp. 1–3.
- [35] G. Stamatelis, K. Stylianopoulos, and G. C. Alexandropoulos, "Evolving multi-branch attention convolutional neural networks for online RIS configuration," *IEEE Trans. Cogn. Commun. Netw.*, pp. 1–1, 2025.
- [36] J.-J. Sun, S. Sun, Y. P. Chen, L. Jiang, and others., "Machine-learning-based hybrid method for the multilevel fast multipole algorithm," *IEEE Antennas Wireless Propag. Lett.*, vol. 19, no. 12, pp. 2177–2181, Dec. 2020.
- [37] G. Barton, *Elements of Green's Functions and Propagation: Potentials, Diffusion, and Waves*. Oxford, U.K.: Clarendon Press, 1989.
- [38] S. M. Rao, D. R. Wilton, and A. W. Glisson, "Electromagnetic scattering by surfaces of arbitrary shape," *IEEE Trans. Antennas Propag.*, vol. 30, no. 3, pp. 409–418, May 1982.
- [39] M. Cui, J. Long, M. Feng, B. Li, and others., "OctFormer: Efficient octree-based transformer for point cloud compression with local enhancement," in *Proc. 37th AAAI Conf. Artif. Intell.*, vol. 37, 2023, pp. 470–478.

- [40] Y. Saad and M. H. Schultz, "GMRES: A generalized minimal residual algorithm for solving nonsymmetric linear systems," *SIAM J. Sci. Statist. Comput.*, vol. 7, pp. 856–869, 1986.
- [41] H. A. van der Vorst, "Bi-CGSTAB: A fast and smoothly converging variant of Bi-CG for the solution of nonsymmetric linear systems," *SIAM J. Sci. Comput.*, vol. 13, no. 2, pp. 631–644, 1992.
- [42] F. Scarselli, M. Gori, A. C. Tsoi, M. Hagenbuchner, and others., "The graph neural network model," *IEEE Trans. Neural Netw.*, vol. 20, no. 1, pp. 61–80, 2009.
- [43] A. Vaswani, N. Shazeer, N. Parmar, J. Uszkoreit, and others., "Attention is all you need," in *Proc. Adv. Neural Inf. Process. Syst. (NIPS)*, vol. 30, 2017, pp. 5998–6008.
- [44] C. Wen, X. Li, X. Yao, L. Peng, and others., "Airborne LiDAR point cloud classification with global-local graph attention convolution neural network," *ISPRS J. Photogramm. Remote Sens.*, vol. 173, pp. 181–194, Mar. 2021.
- [45] P. Veličković, G. Cucurull, A. Casanova, A. Romero, and others., "Graph attention networks," in *Proc. 6th Int. Conf. Learn. Represent. (ICLR)*, Vancouver, Canada, 2018.
- [46] T. N. Kipf and M. Welling, "Semi-supervised classification with graph convolutional networks," in *Proc. 5th Int. Conf. Learn. Represent. (ICLR)*, Toulon, France, 2017.
- [47] H. Thomas *et al.*, "KPConv: Flexible and deformable convolution for point clouds," in *Proc. IEEE/CVF Int. Conf. Comput. Vis. (ICCV)*, Oct. 2019.
- [48] L. M. Yuan, Y. G. Xu, W. Gao *et al.*, "Design of scale model of plate-shaped absorber in a wide frequency range," *Chin. Phys. B*, vol. 27, no. 4, p. 044101, 2018.
- [49] E. Bauer and R. Kohavi, "An empirical comparison of voting classification algorithms: Bagging, boosting, and variants," *Mach. Learn.*, vol. 36, pp. 105–139, 1999.
- [50] Z. Liu *et al.*, "KAN: Kolmogorov-Arnold networks," *arXiv:2404.19756*, 2024.